Hypervulnerability to Sound Exposure through Impaired Adaptive Proliferation of Peroxisomes.

Sedigheh Delmaghani, Jean Defourny, Asadollah Aghaie, Maryline Beurg, Didier Dulon, Nicolas Thelen, Isabelle Perfettini, Tibor Zelles, Mate Aller, Anaïs Meyer, et al.

To cite this version:

Sedigheh Delmaghani, Jean Defourny, Asadollah Aghaie, Maryline Beurg, Didier Dulon, et al.. Hypervulnerability to Sound Exposure through Impaired Adaptive Proliferation of Peroxisomes.. Cell, 2015, 163 (4), pp.894-906. 10.1016/j.cell.2015.10.023 . pasteur-01230439

HAL Id: pasteur-01230439
https://pasteur.hal.science/pasteur-01230439
Submitted on 18 Nov 2015

Hypervulnerability to sound-exposure through impaired adaptive proliferation of peroxisomes

Sedigheh Delmaghani,[1,2,3] Jean Defourny,[1,2,3] Asadollah Aghaie,[2,3,4] Maryline Beurg,[5] Didier Dulon,[5] Nicolas Thelen,[6] Isabelle Perfettini,[1,2,3] Tibor Zelles,[7,8] Mate Aller,[7] Anaïs Meyer,[1,2,3] Alice Emptoz,[1,2,3] Fabrice Giraudet,[9,10,11] Michel Leibovici,[1,2,3] Sylvie Dartevelle,[12] Guillaume Soubigou,[13] Marc Thiry,[6] E. Sylvester Vizi,[7] Saaid Safieddine,[1,2,3] Jean-Pierre Hardelin,[1,2,3] Paul Avan,[9,10,11,15] and Christine Petit[1,2,3,4,14,15,*]

[1]Unité de Génétique et Physiologie de l'Audition, Institut Pasteur, 75015 Paris, France

[2]UMRS 1120, Institut National de la Santé et de la Recherche Médicale (INSERM), 75015 Paris, France

[3]Sorbonne Universités, UPMC Université Paris 06, Complexité du Vivant, 75005 Paris, France

[4]Syndrome de Usher et Autres Atteintes Rétino-Cochléaires, Institut de la Vision, 75012 Paris, France

[5]Equipe Neurophysiologie de la Synapse Auditive, Université de Bordeaux, Neurosciences Institute, CHU Pellegrin, 33076 Bordeaux, France

[6]Unit of Cell and Tissue Biology, GIGA-Neurosciences, University of Liege, CHU Sart-Tilman, B36, 4000 Liege, Belgium

[7]Institute of Experimental Medicine, Hungarian Academy of Sciences, H-1083 Budapest, Hungary

[8]Department of Pharmacology and Pharmacotherapy, Semmelweis University, H-1089 Budapest, Hungary

[9]Laboratoire de Biophysique Sensorielle, Université d'Auvergne, 63000 Clermont-Ferrand, France

[10]UMR 1107, Institut National de la Santé et de la Recherche Médicale (INSERM), 63000 Clermont-Ferrand, France

[11]Centre Jean Perrin, 63000 Clermont-Ferrand, France

[12]Plateforme d'Ingénierie des Anticorps, Institut Pasteur, 75015 Paris, France

[13]Plateforme Transcriptome et épigénome, Institut Pasteur, 75015 Paris, France

[14]Collège de France, 75005 Paris, France

[15]Co-senior author

*Correspondence: christine.petit@pasteur.fr

SUMMARY :

A deficiency in pejvakin, a protein of unknown function, causes a strikingly heterogeneous form of human deafness. Pejvakin-deficient (*Pjvk*$^{-/-}$) mice also exhibit variable auditory phenotypes. Correlation between their hearing thresholds and the number of pups per cage suggest a possible harmful effect of pup vocalizations. Direct sound or electrical stimulation show that the cochlear sensory hair cells and auditory pathway neurons of *Pjvk*$^{-/-}$ mice and patients are exceptionally vulnerable to sound. Subcellular analysis revealed that pejvakin is associated with peroxisomes, and required for their oxidative stress-induced proliferation. *Pjvk*$^{-/-}$ cochleas display features of marked oxidative stress and impaired anti-oxidant defenses, and peroxisomes in *Pjvk*$^{-/-}$ hair cells show structural abnormalities after the onset of hearing. Noise exposure rapidly upregulates *Pjvk* cochlear transcription in wild-type mice, and triggers peroxisome proliferation in hair cells and primary auditory neurons. Our results reveal that the anti-oxidant activity of peroxisomes protects the auditory system against noise-induced damage.

INTRODUCTION

Mutations of *PJVK*, which encodes pejvakin, a protein of unknown function present only in vertebrates, cause the DFNB59 recessive form of sensorineural hearing impairment. In the first patients described (Delmaghani et al., 2006), the impairment was restricted to neurons of the auditory pathway, with auditory brainstem responses (ABRs) displaying abnormally decreased wave amplitudes and increased inter-wave latencies (Starr and Rance, 2015). ABRs monitor the electrical response of auditory pathways to brief sound stimuli, from the primary auditory neurons synapsing with the sensory cells of the cochlea, the inner hair cells (IHCs), to the colliculus in the midbrain (Møller & Jannetta, 1983). However, some DFNB59 patients were found to have a cochlear dysfunction, as shown by an absence of the otoacoustic emissions (OAEs) that are produced by the outer hair cells (OHCs), frequency-tuned cells endowed with electromotility that mechanically amplify the sound-stimulation of neighboring IHCs (Ashmore, 2008). These patients had truncating mutations of *PJVK*, whereas the previously identified patients, with extant OAEs, had missense mutations (p.T54I or p.R183W) (Ebermann et al., 2007; Schwander et al., 2007; Borck et al., 2011). However, the identification of patients also carrying the p.R183W missense mutation but lacking OAEs (Collin et al., 2007) refuted any straightforward connection between the nature of the *PJVK* mutation and the hearing phenotype. The severity of deafness in DFNB59 patients varies from moderate to profound, and may even be progressive in some patients, suggesting that extrinsic factors may influence the hearing phenotype.

We investigated the role of pejvakin, with the aim of determining the origin of the phenotypic variability of the DFNB59 form of deafness. Our study of *Pjvk* knockout mouse models and of patients revealed an unprecedented hypervulnerability of auditory hair cells and neurons to sound-exposure, accounting for phenotypic variability. We found that pejvakin is a peroxisome-associated protein involved in the oxidative stress-induced proliferation of this organelle. Pejvakin-deficient mice revealed the key role of peroxisomes in the redox homeostasis of the auditory system and in the protection against noise-induced hearing loss.

RESULTS

Heterogeneity in the hearing sensitivity of *Pjvk*$^{-/-}$ mice

We generated pejvakin-null (*Pjvk*$^{-/-}$) mice carrying a deletion of *Pjvk* exon 2 resulting in a frameshift at codon position 71 (p.Gly71*fs**9) (Figure S1 and see Extended Experimental Procedures). ABR thresholds recorded on postnatal day 30 (P30) *Pjvk*$^{-/-}$ mice (n = 48), ranged from 35 to 110 dB SPL (Sound Pressure Level) at 10 kHz but never exceeded 30 dB SPL in their *Pjvk*$^{+/+}$ littermates (n = 26) (Figure 1A). This broad range of hearing sensitivity in *Pjvk*$^{-/-}$ mice, from near-normal hearing to almost complete deafness, extended across the whole frequency spectrum. The thresholds of distortion-product OAEs (DPOAEs) at 10 kHz (i.e. the minimum stimulus required for DPOAEs production by OHCs) also fell within an abnormally large range of values, from 30 to 75 dB SPL, in 28 *Pjvk*$^{-/-}$ mice, indicating an OHC dysfunction, and DPOAEs were undetectable in another 20 *Pjvk*$^{-/-}$ mice, suggesting a complete OHC defect (Figure 1B). The absence of pejvakin in mice thus results in a puzzlingly large degree of hearing phenotype variability.

Hypervulnerability to the natural acoustic environment in *Pjvk*$^{-/-}$ mice

We investigated the variability of *Pjvk*$^{-/-}$ auditory phenotypes, by first determining the ABR thresholds of *Pjvk*$^{-/-}$ littermates from different crosses. Large differences were observed between crosses, with much lesser differences between the *Pjvk*$^{-/-}$ littermates of individual crosses. Litters with larger numbers of pups (6 to 12) had higher ABR thresholds, suggesting that the natural acoustic environment, with the calls of larger numbers of pups, might be deleterious in *Pjvk*$^{-/-}$ mice. Pups are vocally very active from birth to about P20. We manipulated the level of exposure to pup calls by randomly splitting large litters of *Pjvk*$^{-/-}$ pups into groups of 2, 4, 6 and 10 pups per cage, with foster mothers, before P10, i.e. several days before hearing onset. The ABR thresholds at P21 were significantly correlated with the number of pups raised together ($p < 0.001$, $r^2 = 0.51$) (Figure 1C).

We then evaluated the effect on hearing of a controlled sound-stimulation, by presenting 1000 tone bursts at 10 kHz, 105 dB SPL (2-ms plateau stimulations separated by 60-ms intervals of silence), energetically equivalent to a 3-minute stay in the natural environment of a 12-pup litter, while monitoring the ABRs during sound-exposure. These conditions are referred to hereafter as "controlled sound-exposure". We probed the effect of sound exposure by ABR tests which, limited to 50 repetitions of tone bursts, did not influence the hearing thresholds of *Pjvk*$^{-/-}$ mice. In a sample of P30 *Pjvk*$^{-/-}$ mice with initial ABR threshold elevation (below 35 dB SPL), controlled sound-exposure affected ABR thresholds in the 12-20 kHz frequency interval (corresponding to the cochlear zones where hair-cell stimulation was strongest), with an immediate increase of 21.7 ± 10.3 dB ($n = 8$; $p < 0.001$), not observed in *Pjvk*$^{+/+}$ mice (2.2 ± 2.4 dB, $n = 12$; $p = 0.3$) (Figure 1D). *Pjvk*$^{-/-}$ mice transferred to a silent environment after exposure displayed a further increase of 33.7 ± 16.0 dB ($n = 8$) two days after exposure. The threshold shift decreased to 23.7 ± 18.0 dB at seven days, and disappeared entirely by 14 days. When exposed mice were returned to the box with their littermates, their ABR continued to increase, at a rate of 15 dB per week. Pejvakin deficiency thus results in particularly high levels of vulnerability to low levels of acoustic energy, and the increase in ABR thresholds is reversible but only slowly and in a quiet environment.

Hair cells and auditory pathway neurons are affected by pejvakin deficiency

To identify the cellular targets of the pejvakin deficiency, we specifically probed the function of auditory hair cells and neurons in *Pjvk*$^{-/-}$, hair cell-conditional *Pjvk* knockout (*Pjvk*$^{\mathrm{fl/fl}}$Myo15-*cre*$^{+/-}$), and *Pjvk*$^{+/+}$ mice, at the age of three weeks, before and after controlled sound-exposure or controlled electrical simulation. The responses of the IHCs to sound-induced vibrations amplified by OHCs trigger action potentials in the distal part of primary auditory neurons, at the origin of ABR wave-I. In *Pjvk*$^{\mathrm{fl/fl}}$Myo15-*cre*$^{+/-}$ mice, which lack pejvakin only in the hair cells, ABR wave-I amplitude and latency at 105 dB SPL specifically probed IHC function, because IHC responses to such loud sounds are independent of OHC activity (Robles & Ruggero, 2001). The larger wave-I latency (1.58 ms in *Pjvk*$^{\mathrm{fl/fl}}$Myo15-*cre*$^{+/-}$ mice (n = 20) vs. 1.32 ms in *Pjvk*$^{+/+}$ littermates (n = 30); $p < 0.001$) and lower wave-I amplitude (37% of the amplitude in *Pjvk*$^{+/+}$ littermates; $p < 0.001$) suggested a dysfunction of the IHCs. Controlled sound exposure induced further decreases in ABR wave-I amplitude in *Pjvk*$^{-/-}$ and *Pjvk*$^{\mathrm{fl/fl}}$Myo15-*cre*$^{+/-}$ mice (48% and 55% of pre-exposure amplitude, respectively) with respect to *Pjvk*$^{+/+}$ mice (108%; $p < 0.001$ for both comparisons) (Figure 2A), demonstrating that *Pjvk*$^{-/-}$ IHCs are hypervulnerable to sound. As shown above, OHCs are also affected by the pejvakin deficiency. Controlled sound-exposure triggered a mean decrease in the DPOAE amplitude of 16.9 ± 7.2 dB in the 12 to 20 kHz frequency interval in *Pjvk*$^{-/-}$ mice with persistent DPOAEs (n = 8; $p < 0.0001$), and an increase in DPOAE threshold, but it had no effect on the DPOAEs of *Pjvk*$^{+/+}$ mice (n = 9; $p = 0.51$) (Figure 2B). OHCs lacking pejvakin are, thus, also hypervulnerable to sound.

We investigated the effect of the absence of pejvakin on the auditory pathway by comparing electrically evoked brainstem responses (EEBR) in *Pjvk*$^{-/-}$ and *Pjvk*$^{\mathrm{fl/fl}}$Myo15-*cre*$^{+/-}$ mice (see Extended Experimental Procedures). The amplitudes of the most distinctive EEBR waves, E II and E IV, did not differ between the two types of mice (for wave E IV:

2.6 ± 1.8 μV in *Pjvk*$^{-/-}$ mice (n = 18) and 2.2 ± 1.2 μV in *Pjvk*$^{fl/fl}$Myo15-*cre*$^{+/-}$ mice (n = 11); t-test, p = 0.13). However, following controlled electrical exposure at 200 impulses / s for 1 minute, as opposed to electric-impulse stimulation with 16 impulses / s for 10 s for pre- and post-exposure EEBR tests, E II and E IV EEBR wave amplitudes got 41% and 47% smaller, respectively, for at least 3 minutes, in *Pjvk*$^{-/-}$ mice (n = 5; paired t-test, p = 0.02 and p = 0.01, respectively), but were unaffected in *Pjvk*$^{fl/fl}$Myo15-*cre*$^{+/-}$ mice (n = 10; p = 0.83) (Figures 2D, 2G-2I). The E II-E IV interwave interval was 0.41 ms longer in *Pjvk*$^{-/-}$ mice (n = 5) than in *Pjvk*$^{fl/fl}$Myo15-*cre*$^{+/-}$ mice (n = 10; p = 0.003) and controlled electrical exposure extended this interval by a further 0.15 ms in *Pjvk*$^{-/-}$ mice only (paired t-test, p = 0.001) (Figures 2H and 2I). Likewise, Likewise, the latency interval between ABR wave I and wave IV (the counterpart of wave E IV), abnormal in one third of the *Pjvk*$^{-/-}$ mice tested (with an ABR threshold < 95 dB SPL, n = 12) (Figures 2C and 2E), got abnormal in all of them after controlled sound-exposure (0.16 ms further increase; paired t-test, p < 0.001). By contrast, it remained normal in *Pjvk*$^{fl/fl}$Myo15-*cre*$^{+/-}$ mice (n = 10 ears; p = 0.73) (Figures 2C and 2F). Thus the absence of pejvakin affects the propagation of action potentials in the auditory pathway after both controlled electrical and sound-exposure in the *Pjvk*$^{-/-}$ mice.

To clarify whether these abnormalities were of neuronal or glial origin, we performed a rescue experiment in *Pjvk*$^{-/-}$ mice, using adeno-associated virus 8 (AAV8) vector-mediated transfer of the murine pejvakin cDNA (AAV8-Pjvk-IRES-EGFP). AAV8 injected into the cochlea transduces the primary auditory neurons (cochlear ganglion neurons) and neurons of the cochlear nucleus (Figure S2A) but not the hair cells. All *Pjvk*$^{-/-}$ mice (n = 7) injected on P3 and tested on P21 had normal ABR interwave I-IV latencies (Figure 2J), and their EEBR wave-E IV amplitude was insensitive to controlled electrical stimulation (1.91 ± 0.97 μV before and 1.87 μV ± 1.07 after stimulation; paired t-test, p =

0.59) (Figures 2K and 2L). The absence of pejvakin thus renders auditory pathway neurons hypervulnerable to exposure to mild, short stimuli.

Hypervulnerability to sound in DFNB59 patients

We then investigated whether the hearing of DFNB59 patients was also hypervulnerable to sound-exposure. We tested five patients carrying the p.T54I mutation (Delmaghani et al., 2006). Transient-evoked OAEs (TEOAEs) assessing OHC function over a broad range of frequencies were detected for all ears, despite the severe hearing impairment (hearing threshold increasing from 66 dB HL at 250 Hz to 84 dB at 8 kHz). Following minimal exposure to impulse stimuli (clicks at 99 dB nHL), ABR waves were clearly identified in response to 250 clicks. When exposure was prolonged to 1000 clicks (the standard procedure), wave V, the equivalent of mouse ABR-wave IV, which was initially conspicuous, displayed a decrease in amplitude (to 39 ± 30% of its initial amplitude) and an increase in latency (of 0.30 ± 0.15 ms) (Figure 3A, 3C, and 3D). In parallel, the I-V interwave interval increased by 0.30 ± 0.15 ms. Wave-V amplitude and latency recovered fully after 10 minutes of silence (Figure 3B). In control patients with sensorineural hearing impairment of cochlear origin matched for ABR thresholds, similar sound stimulation did not affect ABR wave-V amplitude (105 ± 14% of the initial amplitude after exposure; $n = 13$ patients) or latency (-0.02 ± 0.07 ms change after exposure) (Figures 3C and 3D). Exposure of the DFNB59 patients to 1000 clicks also affected TEOAEs (6.1 ± 5.2 dB nHL decrease in amplitude; paired t-test, $p = 0.02$). Therefore, as in pejvakin-deficient mice, the cochlear and neuronal responses of DFNB59 patients were affected by exposure to low-energy sound.

Redox status abnormalities and ROS-induced cell damage in the cochlea of *Pjvk*$^{-/-}$ mice

We studied the *Pjvk*$^{-/-}$ cochlea by light microscopy on semithin sections, and electron microscopy. On P15 and P21, both OHCs and IHCs were normal in number and shape. Their hair bundles (the mechanoreceptive structures responding to sound), the ribbon synapses of the IHCs and their primary auditory neurons, were unmodified (data not shown). On P30, we observed the loss of a few OHCs (16% ± 11%, n = 5 mice), restricted to the basal region of the cochlea (tuned to high-frequency sounds). From P30 onwards, OHCs, cochlear ganglion neurons, and then IHCs disappeared, and the sensory epithelium (organ of Corti) progressively degenerated (Figure S3).

We investigated possible changes in gene expression in the organ of Corti of P15 *Pjvk*$^{-/-}$ mice, by microarrays (see Extended Experimental Procedures). Eighteen genes had expression levels at least 1.5-fold higher or lower in *Pjvk*$^{-/-}$ mice than in *Pjvk*$^{+/+}$ mice. Marked differences were observed for four genes involved in the redox balance — *CypA*, *Gpx2, c-Dct*, and *Mpv17* — encoding cyclophilin A, glutathione peroxidase 2, c-dopachrome tautomerase, and Mpv17, respectively (Table S1). All these genes were downregulated in *Pjvk*$^{-/-}$ mice, a result confirmed by quantitative RT-PCR (qRT-PCR) (Figure S4A), and all encode anti-oxidant proteins, suggesting that *Pjvk*$^{-/-}$ mice have impaired anti-oxidant defenses (Table S1).

We thus assessed the level of oxidative stress in the cochlea of P21 *Pjvk*$^{-/-}$ mice, by determining the ratio of reduced to oxidized glutathione (GSH:GSSG). The GSSG content was about three times larger than in *Pjvk*$^{+/+}$ mice, whereas the GSH content was 23% smaller, resulting in a GSH:GSSG ratio in *Pjvk*$^{-/-}$ cochleas reduced by a factor of 3.4 (Figure 4A). Pejvakin deficiency thus results in cochlear oxidative stress.

We assessed lipid peroxidation by reactive oxygen species (ROS) in *Pjvk*$^{-/-}$ mice, by immunofluorescence-based detection of the by-product 4-hydroxy-2-nonenal (4-HNE). Strong immunoreactivity was observed in P60 *Pjvk*$^{-/-}$ hair cells and cochlear ganglion neurons (Figure S3B). Quantification of lipid peroxidation in microdissected organs of Corti from P30 *Pjvk*$^{-/-}$ and *Pjvk*$^{+/+}$ mice, showed a moderate but statistically significant increase of the malondialdehyde content in the absence of pejvakin (2.15 ± 0.14 μM in *Pjvk*$^{-/-}$ vs. 1.84 ± 0.11 μM in *Pjvk*$^{+/+}$ mice; p = 0.04). Thus, pejvakin deficiency led to impaired anti-oxidant defenses in the cochlea, resulting in ROS-induced cell damage.

We then studied electrophysiological features of IHCs and OHCs in the mature cochlea of P19-P21 *Pjvk*$^{-/-}$ mice. In IHCs, the number of synaptic ribbons, Ca^{2+} currents, and synaptic exocytosis were unaffected (Figure S5A). We investigated whether *Pjvk*$^{-/-}$ mice display the main K^+ currents found in mature IHCs, specifically $I_{K,f}$, which plays a major part in IHC repolarization and is involved in the high temporal precision of action potentials in postsynaptic nerve fibers, $I_{K,s}$, and $I_{K,n}$ (Oliver et al., 2006). $I_{K,f}$ current that flows through the large conductance voltage- and Ca^{2+}-activated potassium (BK) channels, a well known target of ROS (Tang et al., 2004), was detected in only 4 out of 11 *Pjvk*$^{-/-}$ IHCs, and the mean number of spots immunolabeled for the BK α-subunit per IHC was much lower in *Pjvk*$^{-/-}$ mice (5.0 ± 1.4, n = 283 IHCs from 7 mice) than in *Pjvk*$^{+/+}$ mice (13.9 ± 2.6, n = 204 IHCs from 9 mice; t-test, p < 0.001). By contrast, the $I_{K,s}$ and $I_{K,n}$ currents were not affected (Figure 4B and Figure S5B). The electromotility of OHCs was moderately impaired in *Pjvk*$^{-/-}$ mice (Figure S5C). This contrasted with the total loss of DPOAE in a large majority of *Pjvk*$^{-/-}$ mice from P15 on, even at the highest possible stimulus level of 75 dB SPL. It thus pinpointed the existence of an additional defect, likely a mechanoelectrical transduction defect, the main determinant of DPOAEs at high stimulus levels (Avan et al., 2013). The decrease of the cochlear microphonic potential that reflects mechanoelectrical transduction currents through OHCs of the basal-most cochlear region, indeed corroborated the DPOAE measurements: this potential, recorded for a 5 kHz sound stimulus at 95 dB SPL, was always larger than 10 μV in *Pjvk*$^{+/+}$ mice (n = 8), but fell between 5 μV and 3 μV in the P21

Pjvk$^{-/-}$ mice with residual DPOAEs (n = 2), and below 1 μV, in the *Pjvk*$^{-/-}$ mice without persisting DPOAEs (n = 6). Taken together, oxidative stress in the *Pjvk*$^{-/-}$ cochlea impacts various electrophysiological properties of the hair cells, particularly mechanoelectrical transduction and K^+ current through BK channels.

Mitochondrial defects are a common cause of ROS overproduction. However, we didn't find evidence that mitochondria were damaged, as vulnerability of the mitochondrial membrane potential, $\Delta\psi_m$, to the uncoupler carbonyl cyanide 4-(trifluoromethoxy)phenylhydrazone (FCCP) in the organ of Corti and cochlear ganglion was similar in P17-P30 *Pjvk*$^{-/-}$ and *Pjvk*$^{+/+}$ mice, and analysis of *Pjvk*$^{-/-}$ hair cells by transmission electron microscopy (TEM) revealed no mitochondrial abnormalities (Figure S5D and data not shown).

Pejvakin is a peroxisome-associated protein

By using *Pjvk*$^{-/-}$ cochlea as control, we found that neither the commercially available antibodies nor our initial polyclonal antibody (Delmaghani et al., 2006) specifically recognized pejvakin (data not shown). Given the limited divergence of the pejvakin amino-acid sequence among vertebrates, we tried to elicit an immune response in *Pjvk*$^{-/-}$ mice (see Experimental Procedures). The monoclonal antibody obtained, Pjvk-G21, labeled peroxisomes stained by peroxisome membrane protein 70 (PMP70) antibodies in transfected HeLa cells expressing pejvakin (Figure S6A) and in the human HepG2 hepatoblastoma cell line, which is particularly rich in this organelle (Figure 5A). The specificity of the Pjvk-G21 antibody was demonstrated by the immunolabeling of peroxisomes in the hair cells of *Pjvk*$^{+/+}$, but not *Pjvk*$^{-/-}$ and *Pjvk*$^{fl/fl}$Myo15-*cre*$^{+/-}$ mice (Figure 5B and S6B).

Prediction programs failed to detect the PTS1 or PTS2 motifs in the pejvakin sequence (Mizuno et al., 2008), the targeting signals for the importation of peroxisomal matrix proteins into the organelle (Smith and Aitchison, 2013), suggesting that pejvakin is a peroxisomal membrane or membrane-associated protein.

Structural abnormalities of peroxisomes in the hair cells of *Pjvk*$^{-/-}$ mice

We investigated the distribution and morphology of peroxisomes by TEM. Peroxisomes were identified on the basis of catalase activity detection using 3,3'-diaminobenzidine as substrate. We focused on OHCs, the first to display a dysfunction in *Pjvk*$^{-/-}$ mice. On P30 but not P15, both the distribution and shape of peroxisomes differed between *Pjvk*$^{-/-}$ and *Pjvk*$^{+/+}$ mice (Figure 5E). In *Pjvk*$^{+/+}$ OHCs, the peroxisomes were restricted to an area immediately below the cuticular plate. In *Pjvk*$^{-/-}$ mice, the peroxisomes located just below the cuticular plate were slightly larger than those in *Pjvk*$^{+/+}$ mice. Strikingly, irregular catalase-containing structures, some of which were juxtaposed, were present in the perinuclear region, in the immediate vicinity of the nuclear membrane of all *Pjvk*$^{-/-}$ OHCs, but not of *Pjvk*$^{+/+}$ OHCs (Figure 5E). The lack of pejvakin thus results in peroxisome abnormalities in OHCs after the onset of hearing.

Pejvakin is involved in oxidative stress-induced peroxisome proliferation

In HepG2 cells, protrusions emerging from some peroxisomes, the first step of peroxisome biogenesis from pre-existing peroxisomes, were immunoreactive for pejvakin. String-of-beads structures corresponding to elongated and constricted peroxisomes, preceding final fission (Smith and Aitchison, 2013), were also pejvakin-immunoreactive, suggesting a role of this protein in peroxisome proliferation (Figure S6C). Peroxisomes actively contribute to cellular redox balance, by producing and scavenging/degrading H_2O_2 through a broad spectrum of oxidases and peroxidases (especially catalase), respectively (Schrader and Fahimi, 2006). Because *Pjvk*$^{-/-}$ mice displayed features of marked oxidative stress in the cochlea, we investigated the possible role of pejvakin in peroxisome proliferation in response to oxidative stress induced by H_2O_2 (Lopez-Huertas et al., 2000). Embryonic fibroblasts derived from *Pjvk*$^{+/+}$ and *Pjvk*$^{-/-}$ mice were exposed to H_2O_2 (see Extended Experimental Procedures). In unexposed cells, the number of peroxisomes was similar between the two genotypes (t-test, $p = 0.82$). After H_2O_2 treatment, it increased by 46% in *Pjvk*$^{+/+}$ fibroblasts ($p = 0.004$), but remained unchanged in *Pjvk*$^{-/-}$ fibroblasts ($p = 0.83$), resulting in a statistically significant difference between the two genotypes ($p < 0.001$) (Figures 5C and S7A).

We then asked whether mutations reported in DFNB9 patients also affect peroxisome proliferation. We assessed the number of peroxisomes in transfected HeLa cells producing EGFP alone, EGFP and murine pejvakin, or EGFP and one of the mutated forms of murine pejvakin carrying the mutations responsible for DFNB59 (p.T54I, p.R183W, p.C343S, or p.V330Lfs*7). Cells producing the non-mutated pejvakin had larger numbers of peroxisomes than cells producing EGFP alone, whereas cells producing any of the mutated forms of pejvakin (mutPjvk-IRES-EGFP) had smaller peroxisome numbers. In addition, many of these cells contained enlarged peroxisomes, a feature typical of peroxisome proliferation disorders (Ebberink et al., 2012) (Figure 5D and S7B). Together, these results strongly suggest that pejvakin is directly involved in the production of new peroxisomes from pre-existing peroxisomes.

Upregulation of *Pjvk* cochlear transcription and peroxisome proliferation in response to sound

We then asked whether pejvakin is involved in the physiological response to sound. We first assessed the transcription of *Pjvk*, and of *CypA*, *Gpx2, c-Dct*, and *Mpv17* that were downregulated in *Pjvk*$^{-/-}$ mice, in microdissected organs of Corti from P21 wild-type mice, with or without prior sound-stimulation (5-20 kHz, 105 dB SPL for 1 hour; see Extended Experimental Procedures). Transcript levels were analyzed by qRT-PCR at various times (1, 3, 6, and 18 hours) after sound-exposure (Figure 6A). *Pjvk* transcript levels had increased by factors of 1.9 ± 0.1 and 3.5 ± 0.7, mean ± SEM, after 1 hour and 6 hours, respectively. *CypA*, *c-Dct* and *Mpv17* were also upregulated after 6 hours (by factors of 6.6 ± 1.2, 4.3 ± 0.6 and 1.5 ± 0.1, respectively), as were *c-Fos* and *Hsp70*, used as a positive control, but *Gpx2* was not. Thus, noise-exposure leads to an upregulation of the transcription of *Pjvk* and of genes downregulated in *Pjvk*$^{-/-}$ mice, and this effect is dependent on acoustic energy level (Figure S4B).

This result predicted that sound-exposure would lead to peroxisome proliferation in the auditory system of wild-type mice. Six hours after exposure (5-20 kHz, 105 dB SPL for 1 hour), the numbers of peroxisomes were unchanged (34.5 ± 0.8 and 35.9 ± 1.0, mean ± SEM, per IHC from unexposed and sound-exposed mice, respectively, n = 75 cells from 6 mice; t-test, p = 0.25). However, at 48 hours, they had markedly increased, by a factor of 2.3, in both IHCs and OHCs (84.7 ± 5.0 per IHC and 16.5 ± 1.0 per OHC, n = 90 cells and n = 150 cells from 6 mice, respectively) compared to unexposed mice (36.8 ± 3.0 per IHC and 7.3 ± 0.4 per OHC, n = 90 cells and n = 150 cells from 6 mice, respectively; t-test, $p < 0.0001$ for both comparisons). The number of peroxisomes had also increased, by 35%, in the dendrites of primary auditory neurons (1.7 ± 0.1 and 2.3 ± 0.2 peroxisomes per μm of neurite length, n = 40 neurites from 5 unexposed and 5 sound-exposed *Pjvk*$^{+/+}$ mice, respectively; t-test, p = 0.003) (Figure 6B).

Therapeutic approaches in *Pjvk*$^{-/-}$ mice

Based on these results, we tested whether the classical anti-oxidant drug N-acetyl cysteine (NAC) (either alone or associated with α-lipoic acid and α-tocopherol; see

Extended Experimental procedures), administered to *Pjvk*$^{-/-}$ pups could improve their hearing. The ABR thresholds of P21 NAC-treated *Pjvk*$^{-/-}$ pups (n = 21) were about 10 dB lower than those of untreated *Pjvk*$^{-/-}$ pups (n = 24) for all frequencies tested (t-test, $p < 0.001$ for all comparisons) (Figure 7A). The amplitude of the ABR wave I elicited at 105 dB SPL (4.35 ± 1.16 µV, n = 21), was the same as that of *Pjvk*$^{+/+}$ mice (4.36 ± 1.15 µV, n = 18; t-test, p = 0.97), and greater than that of untreated *Pjvk*$^{-/-}$ mice (1.88 ± 1.07 µV, n = 24; t-test, $p < 0.001$) (Figure 7B). EEBRs were more resistant to the high-rate electrical stimulation in treated than in untreated mutant mice (Figure 7C). Conversely, NAC had no beneficial effect on OHCs (data not shown). The association of NAC with α-lipoic acid and α-tocopherol did not perform any better (data not shown).

Full recovery of the neuronal phenotype was achieved by the intracochlear injection of AAV8-Pjvk-IRES-EGFP (see above). As hair cells are not transduced by AAV8, we investigated whether AAV2/8, which transduces hair cells only (Figure S2B), could rescue the *Pjvk*$^{-/-}$ hair-cell phenotype. The auditory function of *Pjvk*$^{-/-}$ mice (n = 7, four pups per cage in every experiment) receiving intracochlear injections of AAV2/8-Pjvk-IRES-EGFP on P3 was assessed on P21, and the percentage of transduced IHCs and OHCs was evaluated in each injected and contralateral (not injected) cochlea, on the basis of EGFP fluorescence. Improvements in ABR thresholds of 20 to 30 dB SPL with respect to untreated mice were observed for frequencies between 10 and 20 kHz (t-test, $p < 0.001$ for all comparisons; Figure 7D). Upon injection of AAV2/8-EGFP, DPOAEs, ABR thresholds, and ABR wave I amplitude and latency were similar to those of untreated *Pjvk*$^{-/-}$ mice (data not shown). A partial reversion of the OHC dysfunction was obtained, with detectable DPOAEs in pejvakin cDNA-treated cochleas (threshold 54.0 ± 10.7 dB), but not in contralateral, untreated cochleas (Figure 7E). DPOAE thresholds were linearly correlated ($r^2 = 0.74$, $p < 0.001$) with the number of EGFP-tagged OHCs (Figure 7F), suggesting that the normalization of

DPOAE thresholds may be possible if all OHCs could be transduced. The latency of the ABR wave I in response to a 105 dB SPL stimulation decreased significantly (1.38 ± 0.11 ms for the treated ears; $n = 6$, vs. 1.53 ± 0.10 ms for the contralateral, untreated ears; paired t-test, $p = 0.03$) (Figure 7G), and its amplitude increased into the normal range (7.34 ± 0.80 μV vs. 2.93 ± 0.92 μV; paired t-test, $p < 0.001$) (Figure 7H), in relation to the number of EGFP-tagged IHCs ($r^2 = 0.89$ for wave I amplitude, $p < 0.001$; Figure 7I). No correction of the interwave I-IV latency was observed, as expected (data not shown).

Finally, we investigated the effect of the transduction of *Pjvk*$^{-/-}$ IHCs by AAV2/8-Pjvk-IRES-EGFP on their peroxisomes. Before sound-exposure, the numbers of peroxisomes in IHCs of P21 *Pjvk*$^{-/-}$ and AAV2/8-Pjvk-IRES-EGFP injected *Pjvk*$^{-/-}$ mice did not differ from that of *Pjvk*$^{+/+}$ mice (30.5 ± 1.9, 32.3 ± 2.1, and 36.8 ± 3.0 peroxisomes, mean ± SEM per IHC, $n = 60$ cells from 4 *Pjvk*$^{-/-}$ and 4 AAV2/8-Pjvk *Pjvk*$^{-/-}$ mice, and $n = 90$ cells from 6 *Pjvk*$^{+/+}$ mice, respectively; t-test, $p = 0.11$ and $p = 0.30$, respectively). By contrast, 48 hours after sound-exposure (5-20 kHz) at 105 dB SPL for 1 hour, the number of peroxisomes had decreased by 63% in *Pjvk*$^{-/-}$ IHCs (30.5 ± 1.9 and 11.2 ± 1.3 peroxisomes per IHC, $n = 75$ cells from 5 unexposed and 5 sound-exposed *Pjvk*$^{-/-}$ mice, respectively; t-test, $p < 0.0001$), and enlarged PMP70-labeled structures were present close to the nucleus (Figure 7J). In response to the same sound but of a lower intensity, i.e. 97 dB SPL for 1 hour, the number of peroxisomes was unchanged in *Pjvk*$^{-/-}$ IHCs (30.5 ± 1.9 and 34.6 ± 2.3 peroxisomes per IHC, $n = 60$ cells from 4 unexposed and 4 sound-exposed *Pjvk*$^{-/-}$ mice, respectively; t-test, $p = 0.17$), and no enlarged PMP70-stained structures were detected (data not shown). The absence of pejvakin thus resulted in defective sound-induced peroxisomal proliferation (both at 105 dB SPL and 97 dB SPL), and even, in peroxisome degeneration (at 105 dB SPL) in IHCs. In *Pjvk*$^{-/-}$ mice injected with AAV2/8-Pjvk-IRES-EGFP on P3 and exposed to 105 dB SPL for 1 hour on P21, enlarged PMP70-labeled structures were no longer detected in transduced IHCs, and the number of peroxisomes increased by 35% (32.3 ± 2.1 and 43.7 ± 3.0 peroxisomes per IHC, n = 60 cells from unexposed and exposed transduced *Pjvk*$^{-/-}$ IHCs, respectively; t-test, p = 0.002) (Figure 7J). We conclude that pejvakin re-expression fully protects *Pjvk*$^{-/-}$ IHCs from the degenerescence of peroxisomes, and partially restores their impaired adaptive proliferation.

DISCUSSION

Noise-induced hearing loss (NIHL) is the second most common form of sensorineural hearing impairment after presbycusis in the U.S.A. (Dobie, 2008). We describe here a genetic form of NIHL, by showing that pejvakin deficiency in mice and DFNB59 patients leads to hypervulnerability to sound, due to a peroxisomal deficiency. To our knowledge, a peroxisomal cause of an isolated (non-syndromic) form of inherited deafness has not been reported yet. The peroxisome emerges as a key organelle in the redox homeostasis of the auditory system, for coping with the overproduction of ROS induced by high levels of acoustic energy.

Acoustic energy is the main determinant of NIHL. The $L_{EX,8\ hour}$ (for level of exposure over an 8-hour workshift) index has been defined such that an $L_{EX,8\ hour}$ of X dB delivers the same energy as a stable sound of X dB played over a period of eight hours. Chronic occupational exposures to less than 85 dB (or 80 dB, depending on the country) are deemed safe. In *Pjvk*$^{-/-}$ mice, a single exposure to 63 dB $L_{EX,8\ hour}$ increased hearing thresholds by 30 dB, with full recovery occurring after about two weeks. By contrast, a ten-times more energetic exposure to a $L_{EX,8\ hour}$ of 73 dB in wild-type mice of the same strain produces only an 18 dB shift in threshold, with a recovery time of 12 hours (Housley et al., 2013). This hypersensitivity of *Pjvk*$^{-/-}$ mice to noise suggests that the $L_{EX,8\ hour}$ of about 83 dB for a cage of 10 pups is sufficient to account for permanent hearing loss in these *Pjvk*$^{-/-}$

pups, whilst some of those housed in small numbers in quiet rooms can display near-normal hearing thresholds (see Figure 1C). Likewise, the auditory function of DFNB59 patients was transiently affected by a 57 dB $L_{EX,8\ hour}$ exposure, routinely used in ABR tests.

NIHL involves the excessive production of ROS, overwhelming the anti-oxidant defense system and causing irreversible oxidative damage to DNA, proteins, and lipids within the cell (Henderson et al., 2006). Noise-induced oxidative stress results in the production of H_2O_2 and other ROS as by-products, thought to derive from the intense sollicitation of mitochondrial activity, and several mouse mutants with mitochondrial defects are prone to NIHL (Ohlemiller et al., 1999; Brown et al., 2014). Our studies of pejvakin-deficient mouse mutants and rescue experiments targeting the hair cells and auditory neurons unambiguously show that IHCs, OHCs, primary auditory neurons and neurons of the cochlear nucleus are hypervulnerable to sound in the absence of pejvakin, which is consistent with previous results showing that hair cells and neurons of the auditory system are targets of NIHL (Wang et al., 2002; Kujawa & Liberman, 2009; Imig and Durham, 2005). However, our study goes one step further, by implicating a possible common mechanism: peroxisomal failure, the importance of which is demonstrated by the impairment of the redox homeostasis caused by pejvakin deficiency. It also reveals a major cause of the unusually high level of phenotypic variability observed in pejvakin-deficient mice and humans: the difference in sound-exposure and the inability of the peroxisomes to cope with the resulting activity-dependent oxidative stress in the absence of pejvakin. Incidentally, this can account for the apparent paradox that mice carrying the R183W mutation in pejvakin displayed a much more severe neural pathway defect than the *Pjvk*$^{-/-}$ mice (Delmaghani et al., 2006). Due to the preservation of hair cell functions, the auditory neurons of R183W mutant mice should be strongly stimulated, whereas the early permanent damage to cochlear hair cells in *Pjvk*$^{-/-}$ mice acts as a protective "muffler" of the neuronal pathway.

In mammals, the number and metabolic functions of peroxisomes differ between cell types. However, all cell types are able to adapt rapidly to modifications in physiological conditions by changing the number, shape, size, and molecular content of peroxisomes, resulting in considerable functional plasticity of these organelles (Schrader et al., 2012; Smith and Aitchison, 2013). Our experiments on *Pjvk*$^{-/-}$ and *Pjvk*$^{+/+}$ mouse embryonic fibroblasts stressed with H_2O_2 showed that pejvakin is critically involved in the oxidative stress-induced proliferation of peroxisomes through growth and fission of pre-existing peroxisomes. The molecular machinery underlying this adaptive process is still poorly understood beyond the involvement of Pex11α (Li et al., 2002). Of note, the absence of pejvakin only affects the proliferation of peroxisomes from pre-existing peroxisomes, but not the constitutive biogenesis of this organelle. Accordingly, structural abnormalities of peroxisomes in *Pjvk*$^{-/-}$ mice became apparent only after hearing onset, in the context of the oxidative stress produced by noise-exposure. By contrast, the *PEX* gene defects causing Zellweger syndrome spectrum (ZSS) disorders (Waterham & Ebberink, 2012) and rhizomelic chondrodysplasia punctata affect the constitutive biogenesis of peroxisomes. Hearing impairment in ZSS disorders involves a severe impairment of neuronal conduction, and has been attributed to defects in the synthesis of two essential myelin sheath components — plasmalogens and docosahexaenoic acid —, which is critically dependent on peroxisomes. Our results suggest that ZSS also includes a defective redox balance in the hair cells and neurons of the auditory system.

In the context of noise-exposure, the upregulation of *Pjvk* transcription in the cochlea and the subsequent peroxisome proliferation in the hair cells and auditory neurons of wild-type mice suggest that pejvakin-dependent peroxisome proliferation in the auditory system is part of the physiological response to high levels of acoustic energy that result in increased amounts of ROS. This and the marked oxidative stress detected in the *Pjvk*$^{-/-}$ cochlea imply that the proliferation of peroxisomes plays an anti-oxidant role, similar to that reported in other cell types (Santos et al., 2005; Diano et al., 2011). The rapid elevation of the hearing threshold in *Pjvk*$^{-/-}$ mice in response to low-energy sounds and the increase in interwave I-IV latency observed in DFNB59 patients within a few seconds are consistent with an activity-dependent H_2O_2 production that, due to impaired cellular redox homeostasis, results in concentrations of H_2O_2 high enough to impact on the activity of various target proteins including ion channels and transporters (Rice, 2011). The worsening of hearing sensitivity, two days later, in the mutant mice lacking pejvakin, exacerbated by putting back the mice in a noisy environment, fits the picture of the absence of sound-induced biogenesis of peroxisomes (with their degeneration occurring in a high acoustic energy environment). We thus conclude that the hypervulnerability of *Pjvk*$^{-/-}$ mice and DFNB59 patients to sound does not result simply from an exacerbation, by sound, of a pre-existing redox balance defect, but is the consequence of the impaired adaptive proliferation of peroxisomes in the absence of pejvakin. Both the defective peroxisome proliferation in IHCs of *Pjvk*$^{-/-}$ mice in response to sound-exposure and its partial recovery by pejvakin cDNA transfer support this conclusion. A full recovery of the adaptive peroxisome proliferation produced by sound-exposure may require higher concentrations of pejvakin or the sound-induced modulation of *Pjvk* transcription (see Figure 6A), which was missing in our rescue experiments (pejvakin cDNA expression being driven by a constitutive promoter).

In patients with hearing impairment, the amplification of sound by hearing aids or direct electrical stimulation of the auditory nerve by a cochlear implant delivers a stimulus with an energy level similar to that shown here to worsen the hearing impairment of *Pjvk*$^{-/-}$ mice within one minute of sound exposure. Therefore, in cases of peroxisomal deficiency, as in DFNB59, specific protection against redox homeostasis failure is essential. Patients with such conditions should avoid noisy environments and a beneficial effect of hearing devices should require an anti-oxidant protection. N-acetyl cysteine was the only antioxidant drug tested here to display some, albeit limited, efficacy. By contrast, AAV-mediated gene therapy could potentially provide full protection. Finally, deciphering the sound stress-induced protective signaling pathway involving pejvakin, might lead to the discovery of therapeutic agents for NIHL.

EXPERIMENTAL PROCEDURES

Audiological studies in mice

Auditory tests were performed in an anechoic room, on anesthetized animals for which core temperature was maintained at 37°C (see Extended Experimental Procedures).

Audiological tests in patients

Informed consent was obtained from all the subjects included in the study. Pure-tone audiometry was performed, with air- and bone-transmitted tones. Hearing impairment was assessed objectively, by measuring ABRs and transient-evoked otoacoustic emissions (TEOAEs). The nonlinear TEOAE recording procedure was used (derived from the ILO88 system), making it possible to extract TEOAEs from linear reflection artifacts from the middle ear, and to evaluate background noise. TEOAE responses were analyzed in 1 kHz-wide bands centered on 1, 2, 3 and 4 kHz.

Generation of an anti-pejvakin monoclonal antibody

The 3’-end of the coding sequence of the *Pjvk* cDNA (NCBI: NM_001080711.2) was inserted into a pGST-parallel-2 vector (derived from pGEX-4T-1; Amersham). The resulting construct, encoding the C-terminal region of pejvakin (residues 290-352; RefSeq:

NP_001074180.1) fused to an N-terminal glutathione *S*-transferase tag, was introduced into *E. coli* BL21-Gold (DE3) competent cells (Stratagene). The pejvakin protein fragment was purified on a glutathione-Sepharose 4B column, then subjected to size-exclusion chromatography and used as the antigen for immunization. Antibodies were produced by immunizing *Pjvk*$^{-/-}$ mice. An immunoglobulin G monoclonal antibody (K_D of 6 x 10^{-8} M), Pjvk-G21, was selected by ELISA on immunogen-coated plates.

Statistical analyses

Quantitative data are presented as mean ± SD, unless otherwise mentioned. Statistical analyses were performed using GraphPad. Data were analyzed by paired or unpaired Student's t-tests, and, for multiple comparisons, either by one-way or two-way analyses of variance (ANOVA), or by t-tests with the Bonferroni correction. Statistical significance of the differences observed between groups is defined as $p < 0.05$.

ACCESSION NUMBER

The accession number for the transcriptomic data reported in this paper is deposited in GEO: GSE72722.

SUPPLEMENTAL INFORMATION

The supplemental information includes Extended Experimental Procedures, seven figures, and one table.

AUTHOR CONTRIBUTIONS

C.P. and P.A. designed the study. S. Delmaghani designed and performed most of the experiments. S. Dartevelle produced the Pjvk-G21 antibody. G.S. and S. Delmaghani performed the microarray experiments. I.P., J.D., and S. Delmaghani performed the cell biology experiments. N.T., M.T., M.L., S. Delmaghani, and S.S. performed the ultrastructural studies. S. Delmaghani, A.M., and A.E. performed the rescue experiments; M.B. and D.D. performed the *ex vivo* electrophysiology; and P.A. performed the *in vivo* electrophysiology analyses. T.Z., M.A., and E.S.V. studied the mitochondrial membrane potential. C.P., P.A., S. Delmaghani, J.D., and J.-P.H. wrote the manuscript.

ACKNOWLEDGMENTS

We thank M. Aghaie and M. Mobasheri for clinical data, V. Michel for his help in immunohistolabeling, F. Langa-Vives (*Centre d'ingénierie génétique murine* platform) for *Pvjk*$^{fl/fl}$ mice engineering, J. Levilliers for her help in the preparation of the manuscript, J. Thornton and N. Furnham for protein structure prediction and analysis, and M. Ricchetti and P. Aubourg for fruitful discussions. This work was supported by the Louis-Jeantet Foundation, ANR-NKTH "HearDeafTreat" (2010-INTB-1402-23 01 and TÉT_10-1-2011-0421), Fondation Bettencourt Schueller, Fondation Agir pour l'Audition, Humanis Novalis-Taitbout, Réunica-Prévoyance, BNP Paribas, and the French state program ''Investissements d'Avenir'' (ANR-10-LABX-65) (to C.P.).

REFERENCES

Ashmore, J. (2008). Cochlear outer hair cell motility. Physiol. Rev. *88*, 173-210.

Avan, P., Buki, B., and Petit, C. (2013). Auditory distortions: origins and functions. Physiol. Rev. *93*, 1563-1619.

Borck, G., Rainshtein, L., Hellman-Aharony, S., Volk, A.E., Friedrich, K., Taub, E., Magal, N., Kanaan, M., Kubisch, C., Shohat, M*., et al.* (2012). High frequency of autosomal-recessive DFNB59 hearing loss in an isolated Arab population in Israel. Clin. Genet. *82*, 271-276.

Brown, K.D., Maqsood, S., Huang, J.Y., Pan, Y., Harkcom, W., Li, W., Sauve, A., Verdin, E., and Jaffrey, S.R. (2014). Activation of SIRT3 by the NAD(+) precursor nicotinamide riboside protects from noise-induced hearing loss. Cell Metab. *20*, 1059-1068.

Collin, R.W., Kalay, E., Oostrik, J., Caylan, R., Wollnik, B., Arslan, S., den Hollander, A.I., Birinci, Y., Lichtner, P., Strom, T.M*., et al.* (2007). Involvement of DFNB59 mutations in autosomal recessive nonsyndromic hearing impairment. Hum. Mutat. *28*, 718-723.

Delmaghani, S., del Castillo, F.J., Michel, V., Leibovici, M., Aghaie, A., Ron, U., Van Laer, L., Ben-Tal, N., Van Camp, G., Weil, D*., et al.* (2006). Mutations in the gene encoding pejvakin, a newly identified protein of the afferent auditory pathway, cause DFNB59 auditory neuropathy. Nat. Genet. *38*, 770-778.

Diano, S., Liu, Z.W., Jeong, J.K., Dietrich, M.O., Ruan, H.B., Kim, E., Suyama, S., Kelly, K., Gyengesi, E., Arbiser, J.L.*, et al.* (2011). Peroxisome proliferation-associated control of reactive oxygen species sets melanocortin tone and feeding in diet-induced obesity. Nat. Med. *17*, 1121-1127.

Dobie, R.A. (2008). The burdens of age-related and occupational noise-induced hearing loss in the United States. Ear Hear. *29*, 565-577.

Ebberink, M.S., Koster, J., Visser, G., Spronsen, F., Stolte-Dijkstra, I., Smit, G.P., Fock, J.M., Kemp, S., Wanders, R.J., and Waterham, H.R. (2012). A novel defect of peroxisome division due to a homozygous non-sense mutation in the PEX11beta gene. J. Med. Genet. *49*, 307-313.

Ebermann, I., Walger, M., Scholl, H.P., Charbel Issa, P., Luke, C., Nurnberg, G., Lang-Roth, R., Becker, C., Nurnberg, P., and Bolz, H.J. (2007). Truncating mutation of the DFNB59 gene causes cochlear hearing impairment and central vestibular dysfunction. Hum. Mutat. *28*, 571-577.

Henderson, D., Bielefeld, E.C., Harris, K.C., and Hu, B.H. (2006). The role of oxidative stress in noise-induced hearing loss. Ear Hearing *27*, 1-19.

Housley, G.D., Morton-Jones, R., Vlajkovic, S.M., Telang, R.S., Paramananthasivam, V., Tadros, S.F., Wong, A.C., Froud, K.E., Cederholm, J.M., Sivakumaran, Y.*, et al.* (2013). ATP-gated ion channels mediate adaptation to elevated sound levels. Proc. Natl. Acad. Sci. U.S.A. *110*, 7494-7499.

Imig, T.J., and Durham, D. (2005). Effect of unilateral noise exposure on the tonotopic distribution of spontaneous activity in the cochlear nucleus and inferior colliculus in the cortically intact and decorticate rat. J. Comp. Neurol. *490*, 391-413.

Kujawa, S.G., and Liberman, M.C. (2009). Adding insult to injury: cochlear nerve degeneration after "temporary" noise-induced hearing loss. J. Neurosci. *29*, 14077-14085.

Li, X., Baumgart, E., Dong, G.X., Morrell, J.C., Jimenez-Sanchez, G., Valle, D., Smith, K.D. and Gould, S.J. (2002). PEX11alpha is required for peroxisome proliferation in response to 4-phenylbutyrate but is dispensable for peroxisome proliferator-activated receptor alpha-mediated peroxisome proliferation. Mol. Cell. Biol. *22*, 8226-8240.

Lopez-Huertas, E., Charlton, W.L., Johnson, B., Graham, I.A., and Baker, A. (2000). Stress induces peroxisome biogenesis genes. EMBO J. *19*, 6770-6777.

Mizuno, Y., Kurochkin, I.V., Herberth, M., Okazaki, Y., and Schonbach, C. (2008). Predicted mouse peroxisome-targeted proteins and their actual subcellular locations. BMC Bioinform. *9 Suppl 12*, S16.

Møller, A.R., Jannetta, P.J. (1983). Interpretation of brainstem auditory evoked potentials: results from intracranial recordings in humans, Scand. Audiol. *12*, 125-33.

Ohlemiller, K.K., Wright, J.S., and Dugan, L.L. (1999). Early elevation of cochlear reactive oxygen species following noise exposure. Audiol. Neurootol. *4*, 229-236.

Oliver, D., Taberner, A.M., Thurm, H., Sausbier, M., Arntz, C., Ruth, P., Fakler, B., and Liberman, M.C. (2006). The role of BKCa channels in electrical signal encoding in the mammalian auditory periphery. J. Neurosci. *26*, 6181-6189.

Rice, M.E. (2011). H_2O_2: a dynamic neuromodulator. Neuroscientist *17*, 389-406.

Robles, L., and Ruggero, M.A. (2001). Mechanics of the mammalian cochlea. Physiol. Rev. *81*, 1305-1352.

Santos, M.J., Quintanilla, R.A., Toro, A., Grandy, R., Dinamarca, M.C., Godoy, J.A., and Inestrosa, N.C. (2005). Peroxisomal proliferation protects from beta-amyloid neurodegeneration. J. Biol. Chem. *280*, 41057-41068.

Schrader, M., Bonekamp, N.A. and Islinger, M. (2012) Fission and proliferation of peroxisomes. Biochim. Biophys. Acta *1822*, 1343-1357.

Schrader, M., and Fahimi, H.D. (2006). Peroxisomes and oxidative stress. Biochim. Biophys. Acta *1763*, 1755-1766.

Schwander, M., Sczaniecka, A., Grillet, N., Bailey, J.S., Avenarius, M., Najmabadi, H., Steffy, B.M., Federe, G.C., Lagler, E.A., Banan, R., *et al.* (2007) A forward genetics screen in mice identifies recessive deafness traits and reveals that pejvakin is essential for outer hair cell function. J. Neurosci. *27*, 2163-2175.

Smith, J.J., and Aitchison, J.D. (2013). Peroxisomes take shape. Nat. Rev. Mol. Cell Biol. *14*, 803-817.

Starr, A. & Rance, G. (2015). Auditory neuropathy. Handb. Clin. Neurol. *129*, 495-508.

Tang, X.D., Garcia, M.L., Heinemann, S.H., and Hoshi, T. (2004). Reactive oxygen species impair Slo1 BK channel function by altering cysteine-mediated calcium sensing. Nat. Struct. Mol. Biol. *11*, 171-178.

Wang, Y., Hirose, K., and Liberman, M.C. (2002). Dynamics of noise-induced cellular injury and repair in the mouse cochlea. J. Assoc. Res. Otolaryngol. *3*, 248-268.

Waterham, H.R., and Ebberink, M.S. (2012). Genetics and molecular basis of human peroxisome biogenesis disorders. Biochim. Biophys. Acta *1822*, 1430-1441.

FIGURE LEGENDS

Figure 1. Hearing loss variability and greater sensitivity to controlled sound-exposure in *Pjvk*$^{-/-}$ mice. (A) ABR thresholds at 10 kHz in P30 *Pjvk*$^{+/+}$ (n = 26 mice) and *Pjvk*$^{-/-}$ (n = 48 mice) littermates. (B) DPOAE thresholds at 10 kHz in P30 *Pjvk*$^{+/+}$ (n = 14 mice) and *Pjvk*$^{-/-}$ (n = 48 mice) littermates. In ears with no DPOAE, even at 75 dB SPL (the highest sound intensity tested), DPOAE thresholds were arbitrarily set at 80 dB SPL. (C) Relationship between the number of pups raised together (determining sound levels in the immediate environment) and ABR thresholds at 10 kHz in P21 *Pjvk*$^{-/-}$ pups. Inset: Time-frequency analysis of a mouse pup's vocalization. Pup calls from P0 to P21 form harmonic series of about 5 kHz, with the most energetic harmonic at about 10 kHz. In a 12-pup litter, call levels reach 105 ± 5 dB SPL at the entrance to the ear canals of the pups. (D) ABR thresholds at 10 kHz in P30 *Pjvk*$^{+/+}$ and *Pjvk*$^{-/-}$ mice before (dots) and after (crosses) controlled sound-exposure. n.s., not significant; *** $p < 0.001$.

Figure 2. Effects on auditory function of brief exposure to moderately intense stimuli in *Pjvk*$^{+/+}$, *Pjvk*$^{-/-}$, and *Pjvk*$^{fl/fl}$Myo15-*cre*$^{+/-}$ mice. (A-C) ABR wave I amplitude (A), DPOAE amplitude (B) and ABR interwave I-IV latency (C) in *Pjvk*$^{+/+}$, *Pjvk*$^{-/-}$ and *Pjvk*$^{fl/fl}$Myo15-*cre*$^{+/-}$ mice, before (dots) and after (crosses) controlled sound-exposure, revealing the hypervulnerability to sound of both types of cochlear hair cells (IHCs and OHCs) and of the neural pathway. (D) EEBR wave E IV amplitude before and after controlled electrical exposure in *Pjvk*$^{-/-}$ and *Pjvk*$^{fl/fl}$Myo15-*cre*$^{+/-}$ mice, abnormal and hypervulnerable only when pejvakin is absent from auditory neurons (*Pjvk*$^{-/-}$ mice). (E and F) Examples of ABRs in *Pjvk*$^{-/-}$ and *Pjvk*$^{fl/fl}$Myo15-*cre*$^{+/-}$ mice: the latency of wave I is affected by controlled sound-exposure in both mutant mice, and wave IV displays an

additional increase in latency only in *Pjvk*$^{-/-}$ mice. (G-I) Examples of EEBRs in *Pjvk*$^{+/+}$ (G), *Pjvk*$^{-/-}$ (H), and *Pjvk*$^{fl/fl}$Myo15-*cre*$^{+/-}$ (I) mice; EEBRs are affected by controlled electrical exposure only in *Pjvk*$^{-/-}$ mice. (J-L) Neuronal function rescue in *Pjvk*$^{-/-}$ mice by transduction with AAV8-Pjvk: effects on ABR interwave I-IV latency (J), on EEBR wave E IV amplitude and its hypervulnerability to electrical stimulation (K), and on EEBR interwave E II-E IV latency (one example is shown in L, to be compared with H). Vertical arrows indicate the positions of waves I and IV on ABR traces, and of waves E II and E IV on EEBR traces. n.s., not significant; *** $p < 0.001$. Error bars represent the SD. See also Figure S2A.

Figure 3. Hypervulnerability to sound in DFNB59 patients. (A) ABR waves I, III, and V (vertical arrows) in one ear of a patient carrying the *PJVK* p.T54I mutation, in response to 250, 500, and 1000 impulse stimuli (clicks) at 99 dB nHL. (B) Repeated ABRs after 10 minutes of silence, with an even larger vulnerability of waves I, III, and V. (C and D) Distributions of the amplitude (C) and latency (D) of ABR wave V in the tested sample of p.T54I patients ($n = 8$ ears), and in a control group of patients ($n = 13$) with cochlear hearing impairment and matched ABR thresholds, before and after exposure to clicks #250 to #1000. Boxes extend from the 25th to the 75th percentile. Horizontal bars and vertical bars indicate median values and extremes, respectively. Unlike the unaffected controls, all p.T54I patients displayed markedly decreased amplitudes and increased latencies.

Figure 4. Increased oxidative stress and ROS-induced cell damage in the *Pjvk*$^{-/-}$ cochlea. (A) Reduced-glutathione (GSH) (left bar chart), oxidized-glutathione (GSSG) (middle bar chart) contents, and GSH:GSSG ratio (right bar chart), in P21 *Pjvk*$^{-/-}$ versus *Pjvk*$^{+/+}$ cochlea. Error bars represent the SEM of 3 independent experiments. See also Figure

S3. (B) Marked decrease in the BK α-subunit immunolabeling in *Pjvk*$^{-/-}$ IHCs. Left: P20 *Pjvk*$^{+/+}$ and *Pjvk*$^{-/-}$ IHCs. Scale bar is 5 μm. Right: quantitative analysis of BK channel clusters. Error bars represent the SD. See also Figure S5B. * $p < 0.05$, *** $p < 0.001$.

Figure 5. Pejvakin is a peroxisome-associated protein involved in the oxidative stress-induced peroxisomal proliferation. (A, B) Immunolabeling of PMP70 and endogenous pejvakin in a HepG2 cell (A) and in two P20 *Pjvk*$^{+/+}$ IHCs (B). See also Figure S6B. (C) Number of peroxisomes in *Pjvk*$^{+/+}$ and *Pjvk*$^{-/-}$ mouse embryonic fibroblasts (MEFs) subjected to 0.5 mM H_2O_2, versus untreated MEFs (n = 30 cells for each condition). See also Figure S7A. (D) Untransfected HeLa cells (NT), and transfected cells producing either EGFP alone or EGFP together with the wild-type pejvakin (Pjvk) or a mutated Pjvk (p.T54I, p.R183W, p.C343S, or p.V330L*fs**7). Left panel: Bar chart showing the numbers of peroxisome per cell 48 hours after transfection. There were on average 33% more peroxisomes in cells producing both EGFP and Pjvk (n = 200) than in cells producing EGFP alone (n = 150). Right panel: for every range of enlarged peroxisome size, x (0.6-0.8 μm, 0.8-1.0 μm, and > 1.0 μm), in two perpendicular directions, the proportion of cells containing at least one peroxisome. See also Figure S7B. (E) Abnormalities in shape and distribution of peroxisomes in mature *Pjvk*$^{-/-}$ OHCs detected by TEM (P30 *Pjvk*$^{-/-}$ (middle and right panels) and *Pjvk*$^{+/+}$ (left panel) OHCs). Insets (middle panel) show enlarged views of individual peroxisomes. In *Pjvk*$^{+/+}$ OHCs, peroxisomes are grouped just under the cuticular plate (CP) (arrowheads), with none detected in the perinuclear region (n = 33 sections, upper bar chart). In *Pjvk*$^{-/-}$ OHCs, some peroxisomes remain under the CP (arrowheads), but catalase-containing structures, misshapen peroxisomes (arrows), are detected in the perinuclear region (n = 24 sections, upper bar chart). Peroxisomes located under the CP are larger in *Pjvk*$^{-/-}$ OHCs (n = 92 peroxisomes) than in *Pjvk*$^{+/+}$ OHCs (n = 89

peroxisomes) (lower bar chart). N: cell nucleus. ** $p < 0.01$, *** $p < 0.001$. Error bars represent the SEM. Scale bars are 5 μm in (A) and (B), and 0.5 μm in (E).

Figure 6. Effect of exposure to loud sounds on the cochlear expression of *Pjvk* and the number of peroxisomes in cochlear hair cells and ganglion neurons. (A) *Pjvk*, *c-Dct*, *CypA*, *Mpv17*, and *Gpx2* transcript levels assessed by qRT-PCR in P21 *Pjvk*$^{+/+}$ organ of Corti, 1, 3, 6, and 18 hours after sound-exposure (5-20 kHz, 105 dB SPL for 1 hour). The levels of *c-Fos* and *Hsp70* transcripts were used as positive controls. See also Figure S4B. (B) Peroxisome proliferation in P21 *Pjvk*$^{+/+}$ hair cells and cochlear ganglion neurons after sound-exposure (same conditions as in A). Peroxisomes were counted 48 hours after sound-exposure. OHCs, IHCs, and neuronal processes stained for F-actin, myosin VI, and neurofilament protein NF200, respectively. In OHCs and IHCs, the peroxisomes are located below the CP and throughout the cytoplasm, respectively. For OHCs, both a lateral view and a transverse optical section at the level of CP (scheme on the right) are shown. The number of peroxisomes was increased in OHCs, IHCs, and dendrites after sound-exposure. N: cell nucleus. *** $p < 0.001$. Error bars represent the SEM. Scale bars are 5 μm.

Figure 7. Therapeutic approaches in *Pjvk*$^{-/-}$ mice. (A-C) Effect of N-acetyl cysteine (NAC) on auditory function in *Pjvk*$^{-/-}$ mice. (A) ABR thresholds in untreated vs. NAC-treated P21 *Pjvk*$^{-/-}$ mice. (B) ABR wave I amplitude for 10 kHz tone bursts in *Pjvk*$^{+/+}$ and untreated *Pjvk*$^{-/-}$ vs. NAC-treated *Pjvk*$^{-/-}$ mice at P21 (C) EEBR wave E IV amplitude before (dots) and after (crosses) controlled electrical stimulation of the cochlear nerve at 200 impulses/s for 1 minute in *Pjvk*$^{+/+}$, untreated *Pjvk*$^{-/-}$, and NAC-treated *Pjvk*$^{-/-}$ mice. (D-I) Effect of AAV2/8-Pjvk-IRES-EGFP transferred into the cochlear hair cells on the auditory function of *Pjvk*$^{-/-}$ mice. See also Figure S2B. (D) ABR thresholds at 10, 15, and 20 kHz in

AAV2/8-Pjvk-IRES-EGFP treated vs. untreated *Pjvk*$^{-/-}$ mice. (E, H) DPOAE threshold (E) and ABR wave I amplitude (H) at 10 kHz in treated vs. untreated contralateral ears. (G) ABR wave I latency in treated vs. untreated contralateral ears. (F) Correlation between DPOAE thresholds and the proportion of EGFP-tagged (i.e. transduced) OHCs. Six untreated ears have no recordable DPOAE (threshold arbitrarily set at 80 dB SPL, red diamond). (I) Correlation between ABR wave I amplitude at 10 kHz, 105 dB SPL and the percentage of transduced IHCs (EGFP-tagged). (J) Effect of AAV2/8-Pjvk-IRES-EGFP on the peroxisomes in *Pjvk*$^{-/-}$ IHCs. Upper and lower panels show and quantify (bar charts) the peroxisomes in untreated mice 48 hours after sound-exposure (5-20 kHz, 105 dB SPL for 1 hour) (peroxisome abnormalities are indicated by arrowheads). Error bars represent the SD in (A-I), and the SEM in (J). n.s., not significant; * $p < 0.05$, ** $p < 0.01$, *** $p < 0.001$.

Supplemental Information

EXTENDED EXPERIMENTAL PROCEDURES

Animal handling

Animals were housed in the Institut Pasteur animal facilities, which are accredited by the French Ministry of Agriculture for experimentation on live mice (accreditation 75-15-01, issued on September 6th, 2013 in application of the French and European regulations on the care and protection of laboratory animals (EC Directive 2010/63, French Law 2013-118, February 6th, 2013). The corresponding author confirms that the protocols were approved by the veterinary staff of the Institut Pasteur animal facility, and were performed in accordance with the NIH Animal Welfare Insurance #A5476-01 issued on July 31st, 2012.

Gene targeting, genotyping, and RT-PCR

We designed a targeting vector, in which exon 2 of *Pjvk* and the neomycin selection cassette

(Pgk-*neo*) were flanked by loxP sites. A negative selection cassette encoding the diphtheria toxin A fragment was inserted at the 3'-end of the *Pjvk* targeting sequence (Figure S1A). CK35 embryonic stem (ES) cells (Kress et al., 1998), derived from a 129/Sv mouse embryo, were electroporated with the purified, linearized targeting vector, and plated on G418 selective medium, as previously described (Matise et al., 1999). Approximately 300 recombinant ES cell clones were obtained, 12 of which were correctly targeted. The homologous recombinant event was confirmed by PCR, with primers specific for the 5' and 3' genomic sequences outside the region used in the targeting vector, and specific for the Pgk-*neo* sequence. The sequences of the PCR primers used to genotype the floxed *Pjvk* allele are available on request. The integration of the recombinant DNA construct was confirmed by Southern blot analysis and PCR amplification of genomic DNA extracted from mouse tails. Two independent clones were used to create chimeric mice displaying germline transmission, by injection into C57BL/6J blastocysts. Male chimeras were crossed with C57BL/6J females to produce heterozygous animals. Mice heterozygous for the floxed *Pjvk* allele were crossed with Pgk-cre^{m} deleter mice carrying the cre recombinase gene driven by the early-acting ubiquitous phosphoglycerate kinase-1 gene promoter (Lallemand et al., 1998), to obtain *Pjvk*-knockout ($Pjvk^{-/-}$) mice. The targeted deletion of exon 2 was confirmed by PCR analysis.

Mice with a conditional knockout of *Pjvk* ($Pjvk^{fl/fl}$Myo15-$cre^{+/-}$), in which expression of the deleted *Pjvk* was restricted to the inner ear sensory cells, were generated by crossing mice carrying the floxed *Pjvk* allele with transgenic mice expressing the cre recombinase gene under the control of the myosin-15 gene promoter (Caberlotto et al., 2011). Auditory function was analyzed in ubiquitous knockout and conditional knockout mice. All studies were performed in a C57BL/6J-129/Sv mixed genetic background.

For RT-PCR analysis of *Pjvk* transcript levels, total RNA was extracted from the inner ears of *Pjvk*$^{+/+}$ and *Pjvk*$^{-/-}$ P7 mice with the NucleoSpin® RNA II kit (Macherey-Nagel). The sequences of the PCR primers used to characterize the *Pjvk* transcript (Figure S1B) are available on request.

Auditory tests, controlled sound-exposure, and controlled electrical stimulation of the auditory nerve in mice

Mice were anesthetized by intraperitoneal injection of a mixture of ketamine and levomepromazin (100 mg/kg: 5 mg/kg), and their core temperature was maintained at 37°C with the aid of a servo-controlled heating pad. The DPOAE at a frequency $2f_1$-f_2 was recorded in response to two primary tones of similar energy levels, f_1 and f_2, with $f_2/f_1 = 1.20$ (Cub^{e}Dis system, Mimosa Acoustics; ER10B microphone, Etymotic Research). Frequency f_2 was swept at 1/10th octave steps from 4 to 20 kHz, and DPOAE threshold was plotted against frequency f_2 (primary tone levels increased from 20 to 70 dB SPL in 10 dB steps, then to 75 dB SPL). The DPOAE threshold was defined as the smallest primary level leading to a detectable DPOAE. The ABRs in response to calibrated short tone bursts in the 5-40 kHz range (repetition rate 17/s) were derived by the synchronous averaging of electroencephalograms recorded between subcutaneous stainless steel electrodes at the vertex and ipsilateral mastoid, with the help of a standard digital averaging system (CED1401+). A hundred responses to the tone bursts were averaged, except within 10 dB of the ABR threshold (defined as the smallest tone-burst level giving rise to at least one repeatable wave above background noise levels, 150 nV in an anesthetized animal), for which 300 tone bursts were used. Once ABR thresholds had been assessed, ABRs in response to 95 and 105 dB SPL tone bursts (100 averages) were collected for the analysis of suprathreshold ABR waveforms, amplitudes and latencies. Controlled sound-exposure was applied with the same acoustic probe used for ABRs, without moving the sound delivery system, so that pre- and post-exposure ABRs shared the same calibration. The intense stimuli were the same tone bursts used for ABR measurements at 105 dB SPL, presented 1000 times, at the same repetition rate of 17/s.

The eighth cranial nerve was stimulated electrically with a silver electrode placed in the round-window niche and excited by biphasic electrical impulses (neutral electrode in neck muscles; peak amplitude of electrical stimulus about 0.5 V; duration of the positive and negative phases 150 μs; adjustable repetition rate). EEBRs were extracted with the same setup as for ABRs (Roux et al., 2006), in response to 100 electrical impulses presented with alternating polarities (repetition rate 17/s). The EEBR threshold was defined as the smallest electrical amplitude leading to repeatable waves above the level of background noise (the same as for ABRs), labeled from E II to E IV in reference to their ABR equivalents, II-IV (Henry, 1979). Controlled electrical stimulation was applied at 5 dB above the EEBR detection threshold, with a 200 Hz repetition rate. The silver electrode on the round window was occasionally also used to record compound action potentials (CAPs) in response to the same tone bursts used for ABR studies (means of 32 presentations, repetition rate 17/s), before EEBR data collection. These recordings were used to check that CAP thresholds and ABR thresholds were within 2 dB of each other at all frequencies, and the exact position of ABR wave I could be ascertained form the larger wave N1, its equivalent on CAP recordings. This was particularly important in mice with an abnormally small wave I, to prevent incorrect identifications (when wave I was reduced to a very small flattened deflection resembling a summating potential, the slightly larger wave II might have been erroneously labeled wave I on ABR recordings, whereas wave N1, even when small, retained its characteristic shape).

The round-window electrode also provided access to the cochlear microphonic potential (CM), with the same setting used for CAP measurements, except that the stimulus polarity was fixed for CM recordings, instead of alternating between rarefaction and condensation tone-bursts for CAP detection. CM is a far-field potential resulting from mechanoelectrical transduction currents through the OHCs at the basal end of the cochlea, near the collecting electrode, and is an oscillating change in electric potential at the stimulus frequency. Although its shape is closely similar to that of the stimulus that activates the sound-delivering earphone, it was easily separated from a possible electric artefact radiated by the earphone by its delay of about 0.5 ms after stimulus onset, in relation to sound propagation along the tubing system that connected the earphone to the ear canal of the mouse. Its peak-to-peak amplitude was measured for a stimulus of 5 kHz (a frequency much lower than the best frequency of the responding OHCs, so that CM was independent of their electromotility status) presented at 95 dB SPL.

Controlled sound-exposure in DFNB59 patients

We assessed the hypervulnerability to sound of patients, using the minimal sound-exposure leading to ABRs. ABRs were first recorded in response to 250 impulse stimuli (clicks, with a repetition rate of 20/s) at 99 dB above the normal detection threshold (the maximum level with this equipment, a Vivosonic Integrity^{TM} Version 4.50), 20-30 dB above the ABR threshold in the tested ear. The averaging was then extended to 500 and 1000 clicks, and wave identification, amplitudes and latencies post click onset were compared for the three averaged ABRs. In control patients, averaging was prolonged until about 4000 responses to clicks had been collected. After a 10-minute pause with no sound stimulus, the procedure was repeated. TEOAEs were averaged just before the first ABR procedure, then just after, in response to 260 series of clicks presented at 40 dB above the normal detection threshold (these clicks were therefore inaudible in patients).

Recording of mouse vocalizations

The protocol was adapted from that described by Menuet et al. (2011). The mice were placed in a polyethylene cage covered with a metal wire lid. A free field microphone (type 4192, ½-inch, Brüel & Kjaer) was placed 2 cm above the metal lid, in the center of the cage. The microphone output was preamplified (microphone power supply type 2801, Brüel & Kjaer) and digitized by a computer sound card (Dell D830; Dell Inc.) at a sampling rate of 192 kHz. Acoustic vocalizations in the 5-90 kHz frequency range were stored online with Adobe Audition 1.5 software. They were analyzed with software developed in Matlab (The MathWorks Inc., MA) providing a spectrographic display of vocalizations in the time-frequency domain, from which the total vocalization time, mean intensity of vocalizations, and spectral complexity of vocalizations were determined.

Housing of mice in an acoustically quiet environment

As most of the noise to which young mice are exposed is due to vocalizations (Ehret & Riecke, 2002), we split pups from the same litter into three groups, which were then placed in isolated boxes. The pups were separated before P10, corresponding to several days before hearing onset in mice. The boxes were kept in quiet booths, shielded from the sounds emanating from other cages. The cages of the first group contained two mice and a foster mother, those of the second group contained four mice and a foster mother, and those of the third group contained the remaining pups (6 to 10) and their mother.

Determination of total and oxidized glutathione contents

Total glutathione (GSH + GSSG) and oxidized glutathione (GSSG) levels were determined as described by Rahman et al. (2006). Total glutathione and GSSG levels were evaluated by spectrometry at 405 nm. GSH concentration was calculated by subtracting the concentration of GSSG from the total glutathione concentration. Three independent experiments were performed, on the cochlea of P21 *Pjvk*$^{+/+}$ and *Pjvk*$^{-/-}$ mice.

Quantification of lipid peroxidation

We determined the concentration of malondialdehyde, a by-product of lipid peroxidation, with the thiobarbituric acid-reactive substances assay kit (Cayman Chemical Company) and fluorometry at 590 nm. Three independent experiments were performed. For each assay, cochlear sensory epithelia were microdissected from 30 *Pjvk*$^{+/+}$ and 30 *Pjvk*$^{-/-}$ mice.

Plasmids and DNA transfection

The full-length pejvakin cDNA was obtained by RT-PCR on a double-stranded cDNA library prepared from the organs of Corti of P7 C57BL/6 mice. It was inserted into the pIRES2-EGFP vector (Clontech). The mutant pejvakin clones (missense and frameshift mutations) were prepared from the wild-type pejvakin clone with the QuikChange™ Site-Directed Mutagenesis kit (Stratagene). HeLa cells were transiently transfected using Lipofectamine™ 2000 (Invitrogen), according to the manufacturer's instructions.

Treatment of mouse embryonic fibroblasts with H_2O_2

Fibroblasts were isolated from mouse embryos at embryonic day 13.5 and cultured as described by Xu (2005). The cells were incubated in DMEM (Gibco) supplemented with 0.1 mM β-mercaptoethanol, and 0.5 mM H_2O_2 for 4 hours at 37 °C, under normoxic conditions (95% air). The culture medium was then replaced with H_2O_2-free medium. Cell viability was checked 18 hours after H_2O_2 treatment, by measuring mitochondrial reductase activity with the MTT (3-(4,5-dimethylthiazol-2-yl)-2,5-diphenyl tetrazolium bromide) (Sigma M2128) assay. A polyclonal antibody against peroxisome membrane protein 70 (PMP70, Abcam ab3421) was used to label peroxisomes.

AAV-*Pjvk* viral constructs and intracochlear viral transduction

AAV2/8-Pjvk-IRES-EGFP was obtained by inserting the murine pejvakin cDNA flanked by an IRES-EGFP reporter cDNA sequence into the multiple cloning site of the pENN.AAV.CB7.CI.RBG vector (PennVector P1044, Penn Medicine Vector Core - University of Pennsylvania School of Medicine). The virus was produced and titrated by Penn Medicine Vector Core. AAV8-Pjvk was produced by inserting the murine pejvakin cDNA into a single-promoter Ad.MAX™ shuttle vector (ITR-CAG-Dfnb59-WPRE-PolyA-ITR; SignaGen Laboratories). The virus was packaged and titrated by SignaGen Laboratories.

Intracochlear viral transduction was carried out as described by Akil et al. (2012). A fixed volume (2 μl) of a solution containing AAV8-Pjvk or AAV2/8-Pjvk-IRES-EGFP recombinant viruses (10^{13} viral genomes/ml) was gently injected into the perilymphatic compartment of the cochlea through the round window. The pipette was withdrawn, the round window niche was quickly sealed with fascia and adipose tissue, and the bulla was sealed with adhesive tape (3M Vetbond).

Anti-oxidant treatment

All anti-oxidant drugs were purchased from Sigma. A dose of 1% N-acetyl-cysteine, or a cocktail of 0.75% α-lipoic acid, 0.5% α-tocopherol and 1% N-acetyl-cysteine, was added to the drinking water of *Pjvk*$^{-/-}$ mice during and after pregnancy, such that that the *Pjvk*$^{-/-}$ pups received the drug first in utero, and then via breast milk until P21. The auditory function of the pups, raised in groups of four pups per cage, was tested on P21.

Immunofluorescence studies

For the detection of lipid oxidation products in the cochlea by immunohistofluorescence, inner ears were dissected in phosphate-buffered saline (PBS) and fixed by immersion in 4% paraformaldehyde (PFA) in PBS for 2 hours at 4°C. The samples were decalcified by incubation in 10% EDTA in PBS, pH 7.4, for 4 days at 4°C, fixed again in 4% PFA in PBS for 1 hour, rinsed twice in PBS for 10 minutes each, and immersed in 20% sucrose in PBS for 12 hours. They were embedded in Tissue Freezing Medium (Triangle Biomedical Sciences) and frozen. Cryostat sections (12 µm thick) were used for immunohistofluorescence, with an antibody against 4-hydroxy-2-nonenal (1:200, Abcam ab46545).

For brainstem immunohistofluorescence analyses, P21 mice were killed by the injection of a lethal dose of ketamine chlorhydrate, and perfused intravascularly with PBS, followed by 4% PFA in PBS. The brain was excised and fixed in 4% PFA in PBS for 1 hour at 4 °C. The fixed tissues were immersed in 20% sucrose at 4°C overnight, and then frozen in dry ice-cooled isopentane at –30°C to –50°C. Cryostat sections (14 µm thick) were cut and used for immunohistofluorescence analyses.

For whole-mount immunolabeling analyses, the inner ears were fixed in 4% PFA in PBS, and the cochlear sensory areas (organ of Corti) were microdissected. The tissues were rinsed twice in PBS, then permeabilized and blocked by incubation in PBS containing 20% normal goat serum and 0.3% Triton X-100 for 1 hour at room temperature. For GFP detection, whole-mount cochleas were incubated with a mixture of rabbit anti-GFP antibody (1:100, Invitrogen A11122) and chicken anti-GFP antibody (1:100, Abcam ab13970) in 1% bovine serum albumin (BSA) in PBS. A monoclonal antibody against parvalbumin (1:500, Sigma SAB4200545) was used to label auditory neurons. A polyclonal antibody against peroxisome membrane protein 70 (PMP70, 1:100, Abcam ab3421) was used to label peroxisomes. Anti-myosin VI (Roux et al., 2009), anti-ribeye/CtBP2 (Santa Cruz sc-5966), and anti-glutamate receptor 2 (GluR2, Invitrogen 32-0300) antibodies were used to delimit the contours of IHCs, to label and count IHC ribbons, and to label post-synaptic glutamate receptors on the dendritic ends of cochlear ganglion neurons, respectively.

For immunocytofluorescence analyses, HeLa and HepG2 cells were fixed by incubation in 4% PFA in PBS for 15 minutes, washed in PBS, and incubated in 50 mM NH_4Cl, 0.2% Triton X-100 solution for 15 minutes at room temperature. The cells were washed and incubated in 20% normal goat serum in PBS for 1 hour. Cells were incubated with the primary antibody in 1% BSA in PBS for 1 hour. Peroxisomes were labeled with an antibody against PMP70 (1:100, Abcam ab3421). An antibody against mitochondrial import receptor subunit TOMM22 (1:100, Sigma HPA003037) was used to label mitochondria. The mouse monoclonal antibody against pejvakin (Pjvk-G21) was used at 100 μg/ml to determine the subcellular distribution of pejvakin. Cells were then washed in PBS and incubated with the appropriate secondary antibody for 1 hour at room temperature.

For immunofluorescence studies, we used Atto-488- or Atto-647-conjugated goat anti-rabbit IgG (1:500, Sigma 18772, 40839), Atto-550-conjugated goat anti-mouse IgG (1:500, Sigma 43394), and Alexa-Fluor-488-conjugated goat anti-chicken IgG (1:500, Invitrogen A11039) as secondary antibodies. Atto-565 phalloidin (1:700, Sigma 94072) and DAPI (1:7500, Sigma D9542) were used to label actin and cell nuclei, respectively. Images were acquired with a Zeiss LSM700 Meta confocal microscope (Carl Zeiss MicroImaging, Inc.). Peroxisomes were counted automatically with the Particles Analysis plugin of ImageJ software (Collins, 2007). Enlarged peroxisomes were identified by measurements in two perpendicular directions, with ImageJ software.

Morphological analyses and peroxisome staining

For scanning electron microscopy studies, mouse inner ears of P15 and P30 mice were fixed by perfusion of the perilymphatic compartment with 2.5% phosphate-buffered glutaraldehyde, and rinsed in PBS. Cochleas were then microdissected, dehydrated in graded ethanol solutions, and dried to critical point. Processed specimens were then mounted on aluminum stubs with colloidal silver adhesive, and sputter-coated with gold palladium before imaging in a JSM-6700 F Jeol scanning electron microscope. Inner ears from 10 *Pjvk*$^{+/+}$ mice (three at P15, four at P30, and three at P60), and 12 *Pjvk*$^{-/-}$ mice (three at P15, five at P30, and four at P60) were analyzed.

For transmission electron microscopy studies, cochleas were prepared as previously described (Thelen et al., 2009). They were fixed by incubation in 2.5% glutaraldehyde in 0.1 M Sörensen's buffer, pH 7.4, for 2 hours at 4°C. After several washes in 0.1 M Sörensen's buffer (pH 7.4), the samples were postfixed by incubation at 4°C with 2% osmium tetroxide in the same buffer for 1 hour. The selective staining of peroxisomes was carried out by a modified version of a published method (Angermüller & Fahimi, 1981). Briefly, the cochleas were fixed by incubation in 1% glutaraldehyde in 0.1 M cacodylate buffer, pH 7.2, at 4°C for 1 hour. After several washes in this buffer, the samples were immersed in 10 mM 3,3'-diaminobenzidine (DAB) and 0.15% H_2O_2 in 0.05 M Teorell-Stenhagen buffer (57 mM boric acid, 50 mM phosphoric acid, 35 mM citric acid, 345 mM NaOH), pH 10.5, for 45 minutes at 30°C. After several washes in the same buffer, the samples were postfixed by incubation with 2% osmium tetroxide in H_2O for 1 hour at 4°C. All the cochleas were then washed in deionized water, dehydrated in graded ethanol solutions, and embedded in Epon (Epon-812, Electron Microscopy Sciences) for 48 hours at 60°C.

Ultrathin sections (70 nm thick) were obtained with an ultramicrotome (Reichert Ultracut E) equipped with a diamond knife (Diatome). The sections were mounted on copper grids coated with collodion. Sections for morphological analysis were contrast-stained with uranyl acetate and lead citrate, for 15 minutes each. The ultrathin sections were observed under a JEM-1400 transmission electron microscope (Jeol) at 80 kV, and photographed with an 11 MegaPixel bottom-mounted TEM camera system (Quemesa, Olympus). The images were analyzed with iTEM software (Olympus). The quantitative data were obtained with the same software.

Acoustic exposure for the quantification of cochlear transcripts and peroxisomes

Three-week-old C57Bl/6 wild-type mice were used. In the first set of experiments, the animals were exposed to overstimulation for one hour with bandpass-filtered white noise, the spectrum of which covered the 5-20 kHz interval with an intensity of 105 dB SPL. Both transcripts and peroxisomes were quantified. In the second set of experiments, in which only transcripts were quantified, the mice were subjected to bandpass-filtered white noise with a spectrum covering the 5-20 kHz interval, but a lower intensity (90 dB SPL), for 1 hour. The white noise signal was generated with in-house Matlab software (The Mathworks), and was delivered by an amplifier to a set of four Ultrasonic Vifa speakers (Avisoft Bioacoustics). The speakers were attached to the tops of four custom-made, cylindrical sound-isolation chambers (15 cm in radius), in which the mice were enclosed. The noise intensity delivered by the speakers was calibrated with a BK4812 probe (Bruel & Kjaer) placed centrally on the lower surface of the isolation chambers. The sound field within each chamber varied by less than 10 dB over the lower surface.

Microarray analysis and quantitative RT-PCR

Total RNA was extracted from dissected organs of Corti of *Pjvk*$^{-/-}$ and wild-type (*Pjvk*$^{+/+}$) P15 mice in Trizol reagent (Invitrogen), purified on RNeasy columns (Qiagen), and tested on an Agilent (Waldbronn) 2100 Bioanalyzer. Three biological replicates were run for each genotype. The cRNAs obtained from 100 ng of RNA were amplified with the GeneChip Expression Two-Cycle 3’ amplification system (Affymetrix). Fragmented biotin-labeled cRNA samples were hybridized to Affymetrix Mouse Gene ST 1.0 arrays. The array was then washed and stained according to the Affymetrix protocol. The stained array was scanned at 532 nm with an Affymetrix GeneChip Scanner 3000, producing CEL files. Gene expression levels were estimated from the CEL file probe-level hybridization intensities with the model-based Robust Multichip Average algorithm (Bolstad et al. 2003). Arrays were compared in local pool error tests (Jain et al., 2003), and the p values were adjusted with the Benjamini–Hochberg algorithm (Benjamini & Hochberg, 1995). The fold differences reflect the relative expression levels of the genes in the organs of Corti of *Pjvk*$^{-/-}$ mice normalized with respect to *Pjvk*$^{+/+}$ mice.

The differences in *Mpv17*, *c-Dct*, *Gpx2*, *CypA*, *c-Fos*, and *Hsp70* transcript levels between sound-exposed and unexposed cochleas were analyzed by quantitative RT-PCR. For sound-exposed mice, cochleas were collected at 1 hour, 3 hours, 6 hours, and 18 hours after sound-exposure. RNA was extracted from dissected organs of Corti, with the NucleoSpin® RNA II kit (Macherey-Nagel). Quantitative RT-PCR was performed with the Universal Probe Library (UPL) system from Roche. UPL probes were labeled with a fluorescein derivative (FAM), and the fluorescence was read with the Applied Biosystems 7500 Real-Time PCR System. The thermocycling conditions were 50°C for 2 minutes, followed by 95°C for 2 minutes, and then 40 cycles of 95°C for 15 s and 60°C for 30 s. Three independent experiments were performed for each sound-exposed or unexposed cochlea. Each assay was conducted for the target transcript probe-set in a multiplex reaction, in which the glyceraldehyde-3-phosphate dehydrogenase (*Gapdh*) probe set was used as an internal control. Relative levels of target transcripts were determined by the comparative cycle threshold (CT) method. The relative copy number for each target transcript was calculated as $2^{-\Delta\Delta CT}$. The sequences of the primers and UPL probes are available on request. Transcription levels in the organ of Corti were compared, for each gene, between sound-exposed and unexposed mice, in unpaired Student's t-tests.

Measurements of synaptic exocytosis and $I_{K,f}$ (BK) current in IHCs, and of non-linear capacitance in OHCs

Experiments were carried out on explants of the organ of Corti. The dissecting-steps were performed in a cold (5-10°C) perilymph-like solution containing (in mM): 135 NaCl, 5.8 KCl, 1.3 $CaCl_2$, 0.9 $MgCl_2$, 0.7 NaH_2PO_4, 5.6 D-glucose, 2 Na pyruvate, and 10 Na-HEPES; pH 7.4 and osmolality near 300 mosmol/kg. The freshly dissected sensory organ was then mounted flat and continuously perfused at room temperature (22-24°C) in a perilymph-like solution. The sensory hair cells were viewed through a X40 LWD water immersion objective (NA = 0.8) on an Olympus BX51WI microscope. Whole-cell voltage clamp recordings were obtained using 3-4 MΩ electrodes pulled from borosilicate glass capillaries (1B150F-4, WPI Sarasota Fl) on a Sachs-Flaming Microelectropuller (Model PC-84, Sutter Instrument Company). Acquisition was done using the Patchmaster software (HEKA).

Ca^{2+} current and exocytosis recordings in IHCs were performed in the perilymph-like solution containing 5 mM Ca^{2+}, and supplemented with 1 µM TTX (Sigma), 10 mM TEA-Cl and 100 nM apamin (Latoxan). The internal pipette solution contained the following (in mM): 150 CsCl, 1 $MgCl_2$, 5 TEA-Cl, 1 EGTA, 5 Na_2ATP, 0.5 Na_2GTP, 5 Cs-HEPES; pH 7.4 and osmolality near 300 mosmol/kg. The liquid junction potential was about 2 mV and was not corrected in our C_m experiments. Real time changes in membrane capacitance (ΔC_m) were measured using the "track-in" circuitry of the HEKA EPC 10 patch clamp amplifier, as previously described (Dulon et al., 2009). A 2.5 kHz sine wave of 15-20 mV was applied to the cells from a holding potential of –80 mV. C_m signals were low-pass filtered at 80 Hz. ΔC_m responses were measured 50 ms after the end of the depolarizing pulse, and averaged over a period of 100 to 300 ms.

For $I_{K,f}$ (BK) current measurement in IHCs, explants were bathed in the perilymph-like solution. The internal solution was a 290 mOsm KCl-based internal solution containing (in mM): 135 KCl, 0.1 $CaCl_2$, 1.5 $MgCl_2$-$6H_2O$, 11 EGTA, 5 HEPES, 2.5 Na_2ATP; pH 7.4. Series resistance (Rs) compensation (50-65%; Rs = 6.34 ± 0.34 MΩ) was applied on line with the series resistance compensation circuitry of the amplifier throughout recordings. To construct the current-voltage curves, $I_{K,f}$ current amplitudes were measured at 1.3 ms after the start of voltage-pulse (from a holding potential of -80 mV) and at the end of the depolarization step. Paxilline, 4-aminopyridine, and XE991 (Tocris Bioscience), blockers of $I_{K,f}$, $I_{K,s}$, and $I_{K,n}$ currents, respectively, were added to the external solution when necessary. Nonlinear capacitance measurements in OHCs were performed as described previously (Santos-Sacchi et al., 1998b).

Imaging of mitochondrial membrane potential in a hemicochlea preparation

We used the hemicochlea preparation described by Dallos and coworkers (Teudt and Richter, 2007). Briefly, P17- P30 mice were lightly anaesthetized with isoflurane gas and decapitated. The cranium was cut in half along the median sagittal axis. The temporal bones were removed and fixed to the stage of a vibrating tissue cutter (Vibratome 3000) with cyanoacrilate glue. Cochleas were then cut in half along the mid modiolar plane with a microtome blade (R35 Feather, Osaka, Japan) under ice-cold modified perilymph (22.5 mM NaCl, 120 mM sodium gluconate, 3.5 mM KCl, 1 mM $CaCl_2$, 1 mM $MgCl_2$, 10 mM HEPES, 5.5 mM glucose). The pH was adjusted to 7.3-7.4, and the solution was saturated with 100 % O_2. The upper half of the cochlea was discarded after cutting. Only the lower parts were used for experiments.

For functional imaging of mitochondrial membrane potential ($\Delta\psi_m$), the hemicochleas were loaded with 5 µM rhodamine 123 (Rh123, Invitrogen) for 5 minutes at room temperature, then washed. When Rh123 is used in the quenched mode, mitochondrial depolarization produces a marked increase in the fluorescence, and $\Delta\psi_m$ changes can be followed reliably (Nicholls and Ward, 2000; Duchen et al., 2003). A perfusion of the protonophore carbonyl cyanide 4-(trifluoromethoxy)phenylhydrazone (FCCP, Sigma) at a concentration of 2 µM was used to trigger $\Delta\psi_m$ collapse.

Hemicochleas were continuously perfused with modified perilymph in an experimental chamber. The perfusion velocity was 3.5 ml/minute, and the solution was 100 % saturated with O_2. All experiments were performed at 36 ± 0.5 ^{o}C. Fluorescent images were obtained with an upright epifluorescent microscope (Olympus BX50WI) equipped with a 4x objective (Olympus XLFluor 4x/340 NA 0.28). With this set up, we were able to image the entire hemicochlea preparation. Oblique illumination was used for orientation purposes. Changes in $\Delta\psi_m$ were observed over the whole section of the cochlear ganglion and organ of Corti in the basal, middle and apical cochlear turns. Rh123 was excited at 495 ± 5 nm with a monochromator equipped with a xenon arc lamp (Polychrome II; T.I.L.L. Photonics GMBH). Emitted light was filtered by a 535/50 band-pass filter (Chroma Technology Corporation) and detected with a cooled CCD camera (Photometrics Quantix), at an image frame rate of 12 images/minute. Image intensities were background-corrected using a nearby area devoid of loaded cells. Axon Imaging Workbench 6 software (Axon Instruments) was used for image acquisition and detailed offline analysis. The data were further analyzed and plotted with Wavemetrics Igor Pro 6. The rise time of the evoked mitochondrial depolarization was determined as the time needed from the start of the response to maximum intensity.

SUPPLEMENTAL FIGURE LEGENDS

Figure S1. Strategy for the targeted replacement of the *Pjvk* wild-type allele with a floxed allele, Related to Figures 1 and 2. (A) Schematic diagram of the murine *Pjvk* gene and the targeting construct used to produce a floxed *Pjvk* allele (*Pjvk*^{fl}) with loxP sequences (triangles) flanking exon 2, followed by a Pgk-*neo* cassette. *DTA*: diphtheria toxin A fragment. An additional *Sac*I site (in bold) was engineered after the first loxP site, for Southern blot analysis. Small arrows indicate the positions of the PCR primers used to screen for clones of recombinant embryonic stem cells. Right panel: Southern blot analysis of *Sac*I-digested genomic DNA from *Pjvk*$^{+/+}$ (+/+) and *Pjvk*$^{fl/+}$ (fl/+) mice. Exon 2 of *Prkra* (a gene flanking *Pjvk,* on the centromeric side) was used as the probe for Southern blot analysis. The probe hybridizes to a 4.6 kb fragment from the floxed allele and a 7.2 kb fragment from the wild-type allele. (B) RT-PCR analysis of the *Pjvk* transcript in the inner ears of P7 *Pjvk*$^{+/+}$ and *Pjvk*$^{-/-}$ mice. *Pjvk*$^{-/-}$ mice were obtained by crossing *Pjvk*$^{fl/fl}$ mice with transgenic mice carrying the cre recombinase gene under the control of the ubiquitous *PGK* promoter. The expected 1059 bp amplicon was detected in the *Pjvk*$^{+/+}$ mouse (lane 1), whereas a 963 bp fragment was detected in the *Pjvk*$^{-/-}$ mouse (lane 2), because of the deletion of exon 2. M, DNA size marker: φX174 DNA *Hae*III digest. See also Figure S6B for validation of the *Pjvk* knockout (*Pjvk*$^{-/-}$) and conditional knockout (*Pjvk*$^{fl/fl}$Myo15-*cre*$^{+/-}$) mouse models at the protein level.

Figure S2. Transduction of neurons in the auditory pathway and of cochlear hair cells with the AAV8 and AAV2/8 viral vectors, respectively, Related to Figures 2J-L and

7D-J. (A-B) AAV8-EGFP or AAV2/8-EGFP was injected into the cochleas of P3 mice, and transduced cells were detected at P21 by EGFP immunostaining (green) on cryosections of the cochlear ganglion (basal turn) (A, lower panel) and of the cochlear nucleus (A, upper panel), and whole-mount preparations of the organ of Corti from the cochlear middle turn (B). The block diagram shows the organ of Corti and the main ascending auditory pathway that projects both ipsilaterally and contralaterally (for the sake of clarity, we show projections from only one cochlea). AAV8-EGFP-transduced auditory neurons are identified by their parvalbumin (red) and EGFP (green) co-immunoreactivity (A). AAV2/8-EGFP transduces the vast majority of inner hair cells (IHCs) and a smaller proportion of outer hair cells (OHCs). The numbers on the DAPI-stained cell nuclei indicate the three rows of OHCs (B). Scale bars are 50 μm in (A) and 10 μm in (B).

Figure S3. Degeneration of the organ of Corti with lipid peroxidation in *Pjvk*$^{-/-}$ mice, Related to Figure 4A. (A) Progressive degeneration of the organ of Corti in *Pjvk*$^{-/-}$ mice. Upper panels: Scanning electron micrographs showing surface views of the organ of Corti in the basal turn of the cochlea from P60 *Pjvk*$^{+/+}$ and *Pjvk*$^{-/-}$ mice. In the *Pjvk*$^{-/-}$ mouse, many outer hair cells (OHCs), inner hair cells (IHCs), and pillar cells (PCs) are missing. Scale bars are 5 μm. Lower panels: Light micrographs of cross sections taken from the middle turn of the cochlea in *Pjvk*$^{+/+}$ and *Pjvk*$^{-/-}$ mice on P90. In the *Pjvk*$^{-/-}$ mouse, OHCs, IHCs, and supporting cells can’t be identified anymore, and the organ of Corti has degenerated (arrow). In addition, the numbers of nerve fibers and cochlear ganglion neurons (arrowheads) are markedly decreased. Scale bars are 80 μm. (B) Increased lipid peroxidation in the cochlea of *Pjvk*$^{-/-}$ mice. Cryosections of the organ of Corti (middle turn, upper panels) and of the cochlear ganglion (apical and basal turns, lower panels) from P60 *Pjvk*$^{+/+}$ and *Pjvk*$^{-/-}$ mice, immunolabeled for 4-HNE, a by-product of lipid peroxidation (green), and stained with

DAPI (blue) to show cell nuclei. Asterisks indicate the nuclei of OHCs and IHCs. In the *Pjvk*$^{-/-}$ mouse, some OHCs and cochlear ganglion neurons are missing, but the OHCs present are highly immunoreactive for 4-HNE (arrows), as are the cochlear ganglion neurons, especially in the basal turn. Scale bars are 20 µm.

Figure S4. Expression levels of genes in *Pjvk*$^{-/-}$ mice and in response to loud sounds in *Pjvk*$^{+/+}$ mice, Related to Figure 6. (A) Quantitative RT-PCR in *Pjvk*$^{-/-}$ mice to confirm microarray results for the genes involved in redox balance. "Fold change" denotes the level of expression of the gene in the organ of Corti of *Pjvk*$^{-/-}$ mice relative to that in *Pjvk*$^{+/+}$ mice, with the minus sign indicating downregulation. All four genes tested, *c-Dct*, *Mpv17*, *CypA*, and *Gpx2*, were less strongly expressed in the organ of Corti of P15 *Pjvk*$^{-/-}$ mice than in *Pjvk*$^{+/+}$ mice, in both microarray (transcriptome) and quantitative RT-PCR (qRT-PCR) analyses. (B) Effect of exposure of wild-type (*Pjvk*$^{+/+}$) mice to loud sound on the expression of *Pjvk* and other anti-oxidant genes in the organ of Corti. Relative levels (fold change) of *Pjvk*, *c-Dct*, *CypA*, *c-Fos*, and *HSP70* transcripts, as measured by quantitative RT-PCR in the organ of Corti of sound-exposed (5-20 kHz, 90 dB for 1 hour) P21 wild-type (*Pjvk*$^{+/+}$) mice after 6 hours in a silent environment versus levels in unexposed mice. Sound-exposure leads to a marked increase in the levels of *Pjvk* and *CypA* transcripts (3.0 ± 0.3-fold and 4.0 ± 1.0-fold, respectively), but only a moderate (less than 2-fold) increase in the levels of *c-Dct, Hsp70*, and *c-Fos* transcripts. This indicates that *Pjvk* and *CypA* are involved in the early cochlear response to noise. Error bars indicate the SEM.

Figure S5. Cochlear physiological characteristics in *Pjvk*$^{-/-}$ mice, Related to Figure 4. (A) Normal number of ribbon synapses and Ca^{2+}-dependent synaptic exocytosis in *Pjvk*$^{-/-}$ inner hair cells (IHCs). Upper panel: The synapses between IHCs and the primary auditory neurons were double-immunolabeled for the presynaptic marker ribeye that labels IHC ribbons (green), and the postsynaptic glutamate receptor GluR2 (red). The bar chart shows the quantitative analysis of ribbon synapses from *Pjvk*$^{+/+}$ (blue) and *Pjvk*$^{-/-}$ (red) mice on P20. N: cell nucleus of IHC. Lower panel: Synaptic function. Left: Bar chart representation of the peak of I_{Ca} and of the increase in membrane capacitance (ΔC_m) in response to a 100 ms voltage step from -80 mV to -10 mV in P20 *Pjvk*$^{+/+}$ (blue) and *Pjvk*$^{-/-}$ (red) IHCs. I_{Ca} and ΔC_m values were similar in *Pjvk*$^{-/-}$ IHCs (126 ± 16 pA and 21.3 ± 2.2 fF, n = 6) and *Pjvk*$^{+/+}$ IHCs (110 ± 16 pA and 20.0 ± 2.0 fF, n = 5; t-test, p = 0.47 and p = 0.64) for I_{Ca} and ΔC_m comparison, respectively. Middle: Synaptic transfer function describing the relation between ΔC_m and I_{Ca} in P20 *Pjvk*$^{+/+}$ (n = 3; blue dots) and *Pjvk*$^{-/-}$ (n = 3; red dots) IHCs. Cells were stimulated by a constant 100 ms voltage step at various membrane potentials from -80 mV to -5 mV. Fits to single data points were done by using a simple power function with N = 0.70 ± 0.10 and N = 0.63 ± 0.10 in *Pjvk*$^{-/-}$ and *Pjvk*$^{+/+}$ IHCs, respectively. The mean slope, representing Ca^{2+} efficiency, was 0.17 ± 0.05 and 0.15 ± 0.02 fF/pA in *Pjvk*$^{-/-}$ IHCs and *Pjvk*$^{+/+}$ IHCs, respectively (t-test, p = 0.73). Right: Increase in membrane capacitance (ΔC_m) produced by a train of 20 successive 100 ms voltage steps from -80 to -10 mV, separated by 100 ms time intervals, in P20 *Pjvk*$^{+/+}$ (n = 3; blue dots) and *Pjvk*$^{-/-}$ (n = 3; red dots) IHCs. *Pjvk*$^{-/-}$ and *Pjvk*$^{+/+}$ IHCs display similar linear increase in membrane capacitance (mean slope of 5.14 ± 0.10 and 5.04 ± 0.35 fF/stimulus in *Pjvk*$^{-/-}$ and *Pjvk*$^{+/+}$ mice, respectively; t-test, p = 0.76). (B) Most *Pjvk*$^{-/-}$ inner hair cells (IHCs) lack the fast voltage-activated $I_{\mathrm{K,f}}$ current. $I_{\mathrm{K,f}}$, $I_{\mathrm{K,s}}$, and $I_{\mathrm{K,n}}$ are the main K^+ currents found in mature IHCs. Upper left: Example traces for potassium currents ($I_{\mathrm{K,f}} + I_{\mathrm{K,s}}$) recorded for a voltage step to -10 mV from a holding potential of -80 mV, in a P19 *Pjvk*$^{+/+}$ (blue) and two P19 *Pjvk*$^{-/-}$ (red) IHCs. Enlarged time scale of the current onset, on the right, shows the fast voltage-activated outward current, $I_{\mathrm{K,f}}$, in the control IHC and one *Pjvk*$^{-/-}$ IHC, whereas in the other *Pjvk*$^{-/-}$ IHC, only a slow current can be observed. Upper middle: Current-voltage (I-V) curves representing mean amplitudes of $I_{K,f}$ (measured 1.3 ms after the onset of the depolarizing pulse, a time point at which $I_{K,s}$ is not yet activated) and of the steady-state current ($I_{K,f} + I_{K,s}$, measured at the end of the voltage step) as a function of the membrane potential (V_m). For *Pjvk*$^{-/-}$ IHCs, two cell groups were defined, based on the presence (open circles) or absence (closed circles) of $I_{K,f}$. Upper right: bar charts showing the mean amplitudes of the $I_{K,f}$ and $I_{K,f} + I_{K,s}$ currents obtained in response to a voltage-step from -80 to -10 mV. $I_{K,f}$ was detected in all 7 IHCs from *Pjvk*$^{+/+}$ mice, but in only four of the 11 IHCs from *Pjvk*$^{-/-}$ mice. The current-voltage relationship at 1.3 ms did not display significantly different conductances in *Pjvk*$^{+/+}$ IHCs (160 ± 20 nS, n = 7) and in the few *Pjvk*$^{-/-}$ IHCs showing $I_{K,f}$ (129 ± 25 nS, n = 4 out of 11), with a mean $I_{K,f}$ amplitude at -10 mV of 1.2 ± 0.2 nA and 0.9 ± 0.3 nA, respectively ($p = 0.53$ for both conductance and amplitude comparisons). Lower left: $I_{K,f}$ blockade with paxilline (10 µM), a selective BK channel blocker, in *Pjvk*$^{+/+}$ and *Pjvk*$^{-/-}$ IHCs submitted to a voltage step from -80 to -10 mV. No current reduction in the presence of paxilline (both at 1.3 ms and steady state plateau) was observed in the *Pjvk*$^{-/-}$ IHCs that displayed only the slow outward current component $I_{K,s}$, indicating that these cells indeed do not have functional BK channels. The amplitudes of $I_{K,s}$ were similar in *Pjvk*$^{+/+}$ and *Pjvk*$^{-/-}$ IHCs (1.76 ± 0.41 nA vs. 1.65 ± 0.24 nA at -10 mV; t-test, $p = 0.6$). Lower middle: Traces representing potassium currents ($I_{K,f} + I_{K,s} + I_{K,n}$) in an IHC from a P19 *Pjvk*$^{-/-}$ mouse. Lower right: Bar chart showing the mean amplitudes of $I_{K,n}$ measured at -120 mV in IHCs from P19 *Pjvk*$^{-/-}$ and *Pjvk*$^{+/+}$ mice. Inward $I_{K,n}$ currents, sensitive to XE991 (30 µM; data not shown), were recorded in all P19-P24 *Pjvk*$^{+/+}$ and *Pjvk*$^{-/-}$ IHCs in response to hyperpolarizing voltage steps from -80 mV to -120 mV, and their amplitudes were similar in the two groups (0.93 ± 0.13 nA vs. 1.3 ± 0.28 nA, respectively; n = 6 in both groups; t-test, $p = 0.3$). Together, these results indicate that *Pjvk*$^{-/-}$ IHCs display normal $I_{K,s}$ and $I_{K,n}$ currents, but most of the cells (64 % of the *Pjvk*$^{-/-}$ IHCs tested) lack the $I_{K,f}$ (BK) current. (C) Impaired electromotility of *Pjvk*$^{-/-}$ OHCs. Left panel: Non-linear capacitance (C_m) of 10 *Pjvk*$^{+/+}$ and 16 *Pjvk*$^{-/-}$ OHCs, as a function of the membrane potential (V_m). Smooth lines are fits based on a two-state Boltzmann function (implemented in JClamp) with values of Q_{max}, $V_{1/2}$, z, and C_{linear} of 1.1 ± 0.9 pC, -33.6 ± 3.5 mV, 0.75 ± 0.05, and 6.6 ± 0.2 pF for *Pjvk*$^{+/+}$ OHCs, and 0.83 ± 0.37 pC, -30.5 ± 1.3 mV, 0.85 ± 0.03, and 7 ± 0.3 pF for *Pjvk*$^{-/-}$ OHCs, respectively. Right panel: Bar chart showing a 30% mean decrease of maximal charge density ($Q' = Q/C_{linear}$) in *Pjvk*$^{-/-}$ OHCs. (D) Dissipation of the $\Delta\psi_m$ revealed no difference in mitochondrial status between *Pjvk*$^{+/+}$ and *Pjvk*$^{-/-}$ cochleas. Functional imaging of $\Delta\psi_m$ was performed over sections of the organ of Corti and cochlear ganglion, in turns of the hemicochlea of P17-P30 *Pjvk*$^{+/+}$ and *Pjvk*$^{-/-}$ mice (n = 12 ears for each genotype), after loading the preparation by Rh123. A perfusion of the protonophore FCCP was used to trigger $\Delta\psi_m$ collapse. The starting latencies (SL) of the response and rise times (RT) of the evoked depolarization peaks were calculated and compared. The inset graphs demonstrate the way of determination of SL and RT on a representative trace. In the bar charts, basal, middle, and apical denote cochlear turns. The six regions of interest are delimited by black borders on the insets showing the fluorescent and obliquely illuminated images of a hemicochlea.

Error bars represent the SD in (A-C), and the SEM in (D). n.s., not significant, *** $p < 0.001$.

Figure S6. Pejvakin immunostaining of peroxisomes, Related to Figure 5. (A) Pejvakin is associated with peroxisomes in transfected HeLa cells. Transfected HeLa cells producing pejvakin (Pjvk-EGFP, upper panel) and untransfected cells (lower panel) were immunostained with both an anti-pejvakin antibody (Pjvk-G21) and an antibody against peroxisome membrane protein 70 (PMP70). Cell nuclei were stained with DAPI (blue).

Colocalization of the immunostainings of pejvakin (red) and PMP70 (green) was observed in transfected cells (see inset for higher magnification of the boxed area). Pejvakin was not detected in untransfected cells. (B) Absence of immunolabeling in inner hair cells (IHCs) from P21 *Pjvk*$^{-/-}$ and *Pjvk*$^{\mathrm{fl/fl}}$Myo15-*cre*$^{+/-}$ mice with the Pjvk-G21 antibody demonstrates the specificity of this antibody (see Figure 5B for immunolabeling in *Pjvk*$^{+/+}$ IHCs). (C) Pejvakin immunostaining of dividing peroxisomes. Double immunolabeling of HepG2 cells for pejvakin (red) and PMP70 (green). Upper panel: arrowheads indicate pejvakin-immunoreactive protrusions from pre-existing peroxisomes. Lower panel: boxed areas show pejvakin-immunoreactive string-of-beads structures corresponding to elongated and constricted peroxisomes (preceding final fission). Scale bar is 10 μm in (A), 5 μm in (B), and 2 μm in (C).

Figure S7. Pejvakin-dependent peroxisomal proliferation, Related to Figure 5. (A) Proliferation of peroxisomes induced by H_2O_2 in *Pjvk*$^{+/+}$ mouse embryonic fibroblasts. F-actin (red), PMP70 (green), and DAPI (blue) staining of *Pjvk*$^{+/+}$ (left panel) and *Pjvk*$^{-/-}$ (right panel) mouse embryonic fibroblasts (MEFs), treated with 0.5 mM H_2O_2 for 4 hours or left untreated, and analyzed 18 hours later. H_2O_2-treatment increases the number of peroxisomes only in the *Pjvk*$^{+/+}$ cells (see quantification in Figure 5C). (B) Larger numbers and enlargement of peroxisomes in transfected HeLa cells producing wild-type and mutant forms of pejvakin, respectively. In cells producing EGFP alone, EGFP and wild-type pejvakin (Pjvk), or EGFP and the p.T54I, p.R183W, p.C343S, or p.V330L*fs**7 mutated forms of pejvakin, peroxisomes were identified on the basis of their PMP70-immunoreactivity. The upper panel shows F-actin (red), DAPI (dark blue), EGFP (green), and PMP70 (light blue) staining, whereas the lower panel shows only the PMP70 immunostaining of individual cells delimited by a white border. The number of peroxisomes is larger in cells producing wild-type pejvakin, and smaller in the cells producing any of the mutated forms of pejvakin, than in cells producing EGFP alone (see quantification in Figure 5D). In addition, cells producing the mutated forms of pejvakin contain enlarged peroxisomes (arrowheads, and see insets for magnification; see also quantification in Figure 5D). Scale bar is 20 μm in (A) and 10 μm in (B).

SUPPLEMENTAL REFERENCES

Akil, O., Seal, R.P., Burke, K., Wang, C., Alemi, A., During, M., Edwards, R.H., and Lustig, L.R. (2012). Restoration of hearing in the VGLUT3 knockout mouse using virally mediated gene therapy. Neuron *75*, 283-293.

Angermuller, S., and Fahimi, H.D. (1981). Selective cytochemical localization of peroxidase, cytochrome oxidase and catalase in rat liver with 3,3'-diaminobenzidine. Histochemistry *71*, 33-44.

Benjamini, Y., and Hochberg, Y. (1995). Controlling the false discovery rate: a practical and powerful approach to multiple testing. J. Roy. Statist. Soc. Ser. B *57*, 289-300.

Benlloch, S., Galbis-Caravajal, J.M., Alenda, C., Peiro, F.M., Sanchez-Ronco, M., Rodriguez-Paniagua, J.M., Baschwitz, B., Rojas, E., and Massuti, B. (2009). Expression of molecular markers in mediastinal nodes from resected stage I non-small-cell lung cancer (NSCLC): prognostic impact and potential role as markers of occult micrometastases. Ann. Oncol. *20*, 91-97.

Binder, C.J., Weiher, H., Exner, M., and Kerjaschki, D. (1999). Glomerular overproduction of oxygen radicals in Mpv17 gene-inactivated mice causes podocyte foot process flattening and proteinuria: A model of steroid-resistant nephrosis sensitive to radical scavenger therapy. Am. J. Pathol. *154*, 1067-1075.

Bingle, L., Cross, S.S., High, A.S., Wallace, W.A., Devine, D.A., Havard, S., Campos, M.A., and Bingle, C.D. (2005). *SPLUNC1* (*PLUNC*) is expressed in glandular tissues of the respiratory tract and in lung tumours with a glandular phenotype. J. Pathol. *205*, 491-497.

Bolstad, B.M., Irizarry, R.A., Astrand, M., and Speed, T.P. (2003). A comparison of normalization methods for high density oligonucleotide array data based on variance and bias. Bioinformatics *19*, 185-193.

Caberlotto, E., Michel, V., Foucher, I., Bahloul, A., Goodyear, R.J., Pepermans, E., Michalski, N., Perfettini, I., Alegria-Prevot, O., Chardenoux, S., *et al.* (2011). Usher type 1G protein sans is a critical component of the tip-link complex, a structure controlling actin polymerization in stereocilia. Proc. Natl. Acad. Sci. U.S.A. *108*, 5825-5830.

Collins, T.J. (2007). ImageJ for microscopy. BioTechniques *43*, 25-30.

de Pril, R., Hobo, B., van Tijn, P., Roos, R.A., van Leeuwen, F.W., and Fischer, D.F. (2010). Modest proteasomal inhibition by aberrant ubiquitin exacerbates aggregate formation in a Huntington disease mouse model. Mol. Cell. Neurosci. *43*, 281-286.

Duchen, M.R., Surin, A., and Jacobson, J. (2003). Imaging mitochondrial function in intact cells. Methods Enzymol. *361*, 353-389.

Dulon, D., Safieddine, S., Jones, S.M., Petit, C. (2009). Otoferlin is critical for a highly sensitive and linear calcium-dependent exocytosis at vestibular hair cell ribbon synapses. J Neurosci. *29*, 10474-87.

Ehret, G., and Riecke, S. (2002). Mice and humans perceive multiharmonic communication sounds in the same way. Proc. Natl. Acad. Sci. U.S.A. *99*, 479-482.

Evans, P., and Halliwell, B. (1999). Free radicals and hearing. Cause, consequence, and criteria. Ann. N. Y. Acad. Sci. *884*, 19-40.

Fischer, D.F., De Vos, R.A., Van Dijk, R., De Vrij, F.M., Proper, E.A., Sonnemans, M.A., Verhage, M.C., Sluijs, J.A., Hobo, B., Zouambia, M., *et al.* (2003). Disease-specific accumulation of mutant ubiquitin as a marker for proteasomal dysfunction in the brain. FASEB J. *17*, 2014-2024.

Ge, Y.S., Teng, W.Y., and Zhang, C.D. (2009). Protective effect of cyclophilin A against Alzheimer's amyloid beta-peptide (25-35)-induced oxidative stress in PC12 cells. Chin. Med. J. *122*, 716-724.

Hallen, L.C., Burki, Y., Ebeling, M., Broger, C., Siegrist, F., Oroszlan-Szovik, K., Bohrmann, B., Certa, U., and Foser, S. (2007). Antiproliferative activity of the human IFN-alpha-inducible protein IFI44. J. Interferon Cytokine Res. *27*, 675-680.

He, Y., Zhou, G., Zhai, Y., Dong, X., Lv, L., He, F., and Yao, K. (2005). Association of *PLUNC* gene polymorphisms with susceptibility to nasopharyngeal carcinoma in a Chinese population. J. Med. Genet. *42*, 172-176.

Henry, K.R. (1979). Auditory brainstem volume-conducted responses: origins in the laboratory mouse. J. Am. Aud. Soc. *4*, 173-178.

Jain, N., Thatte, J., Braciale, T., Ley, K., O'Connell, M., and Lee, J.K. (2003). Local-pooled-error test for identifying differentially expressed genes with a small number of replicated microarrays. Bioinformatics *19*, 1945-1951.

Kanamori, M., Sandy, P., Marzinotto, S., Benetti, R., Kai, C., Hayashizaki, Y., Schneider, C., and Suzuki, H. (2003). The PDZ protein tax-interacting protein-1 inhibits beta-catenin transcriptional activity and growth of colorectal cancer cells. J. Biol. Chem. *278*, 38758-38764.

Kim, K.S., Kang, K.W., Seu, Y.B., Baek, S.H., and Kim, J.R. (2009). Interferon-gamma induces cellular senescence through p53-dependent DNA damage signaling in human endothelial cells. Mech. Ageing Dev. *130*, 179-188.

Kress, C., Vandormael-Pournin, S., Baldacci, P., Cohen-Tannoudji, M., and Babinet, C. (1998). Nonpermissiveness for mouse embryonic stem (ES) cell derivation circumvented by a single backcross to 129/Sv strain: establishment of ES cell lines bearing the Omd conditional lethal mutation. Mamm. Genome *9*, 998-1001.

Lai, M.D., and Xu, J. (2007). Ribosomal proteins and colorectal cancer. Curr. Genomics *8*, 43-49.

Lallemand, Y., Luria, V., Haffner-Krausz, R., and Lonai, P. (1998). Maternally expressed PGK-Cre transgene as a tool for early and uniform activation of the Cre site-specific recombinase. Transgenic Res. *7*, 105-112.

Lee, S.P., Hwang, Y.S., Kim, Y.J., Kwon, K.S., Kim, H.J., Kim, K., and Chae, H.Z. (2001). Cyclophilin a binds to peroxiredoxins and activates its peroxidase activity. J. Biol. Chem. *276*, 29826-29832.

Lu, Y.J., Wu, C.S., Li, H.P., Liu, H.P., Lu, C.Y., Leu, Y.W., Wang, C.S., Chen, L.C., Lin, K.H., and Chang, Y.S. (2010). Aberrant methylation impairs low density lipoprotein receptor-related protein 1B tumor suppressor function in gastric cancer. Gene Chromosomes Cancer *49*, 412-424.

Madjd, Z., Pinder, S.E., Paish, C., Ellis, I.O., Carmichael, J., and Durrant, L.G. (2003). Loss of CD59 expression in breast tumours correlates with poor survival. J. Pathol. *200*, 633-639.

Matise, M.P., Auerbach, W., and Joyner, A. (1999). Production of targeted embryonic stem cell clones. In Gene targeting: a practical approach, A. Joyner, ed. (Oxford: Oxford University Press), pp. 101-132.

Menuet, C., Cazals, Y., Gestreau, C., Borghgraef, P., Gielis, L., Dutschmann, M., Van Leuven, F., and Hilaire, G. (2011). Age-related impairment of ultrasonic vocalization in

Tau.P301L mice: possible implication for progressive language disorders. PLoS One *6*, e25770.

Meyer zum Gottesberge, A.M., Felix, H., Reuter, A., and Weiher, H. (2001). Ultrastructural and physiological defects in the cochlea of the Mpv17 mouse strain. A comparison between young and old adult animals. Hear. Res. *156*, 69-80.

Michard, Q., Commo, S., Belaidi, J.P., Alleaume, A.M., Michelet, J.F., Daronnat, E., Eilstein, J., Duche, D., Marrot, L., and Bernard, B.A. (2008a). TRP-2 specifically decreases WM35 cell sensitivity to oxidative stress. Free Radic. Biol. Med. *44*, 1023-1031.

Michard, Q., Commo, S., Rocchetti, J., El Houari, F., Alleaume, A.M., Wakamatsu, K., Ito, S., and Bernard, B.A. (2008b). TRP-2 expression protects HEK cells from dopamine- and hydroquinone-induced toxicity. Free Radic. Biol. Med. *45*, 1002-1010.

Nakagawa, T., Pimkhaokham, A., Suzuki, E., Omura, K., Inazawa, J., and Imoto, I. (2006). Genetic or epigenetic silencing of low density lipoprotein receptor-related protein 1B expression in oral squamous cell carcinoma. Cancer Sci. *97*, 1070-1074.

Nicholls, D.G., and Ward, M.W. (2000). Mitochondrial membrane potential and neuronal glutamate excitotoxicity: mortality and millivolts. Trends Neurosci. *23*, 166-174.

Rahman, I., Kode, A., and Biswas, S.K. (2006). Assay for quantitative determination of glutathione and glutathione disulfide levels using enzymatic recycling method. Nat. Protoc. *1*, 3159-3165.

Roux, I., Hosie, S., Johnson, S.L., Bahloul, A., Cayet, N., Nouaille, S., Kros, C.J., Petit, C., and Safieddine, S. (2009). Myosin VI is required for the proper maturation and function of inner hair cell ribbon synapses. Hum. Mol. Genet. *18*, 4615-4628.

Roux, I., Safieddine, S., Nouvian, R., Grati, M., Simmler, M.-C., Bahloul, A., Perfettini, I., Le Gall, M., Rostaing, P., Hamard, G*., et al.* (2006). Otoferlin, defective in a human deafness form, is essential for exocytosis at the auditory ribbon synapse. Cell *127*, 277-289.

Santos-Sacchi, J., Kakehata, S., Takahashi, S. (1998b). Effects of membrane potential on the voltage dependence of motility-related charge in outer hair cells of the guinea-pig. J. Physiol. *510*, 225–235.

Schenk, T., Stengel, S., Goellner, S., Steinbach, D., and Saluz, H.P. (2007). Hypomethylation of *PRAME* is responsible for its aberrant overexpression in human malignancies. Gene Chromosomes Cancer *46*, 796-804.

Sonoda, I., Imoto, I., Inoue, J., Shibata, T., Shimada, Y., Chin, K., Imamura, M., Amagasa, T., Gray, J.W., Hirohashi, S*., et al.* (2004). Frequent silencing of low density lipoprotein receptor-related protein 1B (LRP1B) expression by genetic and epigenetic mechanisms in esophageal squamous cell carcinoma. Cancer Res. *64*, 3741-3747.

Spinazzola, A., Viscomi, C., Fernandez-Vizarra, E., Carrara, F., D'Adamo, P., Calvo, S., Marsano, R.M., Donnini, C., Weiher, H., Strisciuglio, P*., et al.* (2006). *MPV17* encodes an inner mitochondrial membrane protein and is mutated in infantile hepatic mitochondrial DNA depletion. Nat. Genet. *38*, 570-575.

Teudt, I.U., and Richter, C.P. (2007). The hemicochlea preparation of the guinea pig and other mammalian cochleae. J. Neurosci. Methods *162*, 187-197.

Thelen, N., Breuskin, I., Malgrange, B., and Thiry, M. (2009). Early identification of inner pillar cells during rat cochlear development. Cell Tissue Res. *337*, 1-14.

Tu, S., Shin, Y., Zago, W.M., States, B.A., Eroshkin, A., Lipton, S.A., Tong, G.G., and Nakanishi, N. (2007). Takusan: a large gene family that regulates synaptic activity. Neuron *55*, 69-85.

Watson, N.F., Durrant, L.G., Madjd, Z., Ellis, I.O., Scholefield, J.H., and Spendlove, I. (2006). Expression of the membrane complement regulatory protein CD59 (protectin) is associated with reduced survival in colorectal cancer patients. Cancer Immunol. Immunother. *55*, 973-980.

Wool, I.G. (1996). Extraribosomal functions of ribosomal proteins. Trends Biochem. Sci. *21*, 164-165.

Xu, J. (2005). Preparation, culture, and immortalization of mouse embryonic fibroblasts. In Current Protocols in Molecular Biology. *70*, 28.1:28.1.1–28.1.8.

Table S1. Transcriptional changes in the organ of Corti of *Pjvk*$^{-/-}$ mice, Related to Figure 6A.

Gene (encoded protein)	**Accession number**	**Fold change**	**Adjusted p-value**	**Probe set**	**References**
Genes involved in ROS metabolism					
Mpv17 (Mpv17, mitochondrial inner membrane protein)	NM_008622	-3.40	3.34E-22	10529091	Binder et al, 1999; Meyer zum Gottesberge, 2001; Spinazzola et al., 2006
c-Dct (c-Dopachrome tautomerase)	NM_010024	-3.28	9.95E-50	10422249	Michard et al., 2008a; Michard et al., 2008b
CypA (Cyclophilin A)	NM_008907	-2.15	1.78E-09	10545337	Lee et al., 2001; Ge et al., 2009
Gpx2 (Glutathione peroxidase 2)	NM_030677	-1.59	4.87E-11	10401109	Evans and Halliwell, 1999
Genes with modified expression in tumors					
Tax1bp3 (Tax1 (human T-cell leukemia virus type I) binding protein 3)	NM_029564	-2.88	2.16E-15	10378334	Kanamori et al., 2003
Plunc (Palate, lung, and nasal epithelium associated protein)	NM_011126	2.20	6.89E-10	10477475	Bingle et al., 2005; He et al., 2005; Benlloch et al., 2009
Cd59a (CD59a antigen)	NM_001111060	-2.13	1.78E-30	10474229	Madjd et al., 2003; Watson et al., 2006
Pramel3 (Preferentially expressed antigen in melanoma-like 3)	NM_031390	-1.94	6.05E-04	10601790	Schenk et al., 2007
Lrp1b (Low density lipoprotein-related protein 1b)	NM_053011	1.82	3.21E-07	10482336	Sonoda et al., 2004; Nakagawa et al., 2006; Lu et al., 2010
Genes encoding putative cell growth inhibitors					
Ifi44 (Interferon-induced protein 44)	NM_133871	-2.20	3.45E-12	10502791	Hallen et al., 2007; Kim et al., 2009
Ifit3 (Interferon-induced protein with tetratricopeptide repeats 3)	NM_010501	-2.08	2.72E-10	10462618	
Ifit1 (Interferon-induced protein with tetratricopeptide repeats 1)	NM_008331	-1.75	1.53E-07	10462623	
Ifitm3 (Interferon-induced transmembrane protein 3)	NM_025378	-1.60	1.42E-11	10569017	

Genes encoding ribosomal proteins					
Rps13 (Ribosomal protein S13)	NM_026533	2.04	5.61E-08	10565434	Wool, 1996; Lai and Xu, 2007
Rps23 (Ribosomal protein S23)	NM_024175	-1.92	1.06E-08	10491730	
Rpl36 (Ribosomal protein L36)	BC086914	-1.74	2.57E-04	10394609	
Gene involved in ubiquitin proteolytic pathway					
UbB (Ubiquitin B)	NM_011664	-1.64	2.93E-07	10376864	Fischer et al., 2003; de Pril et al., 2010
Gene encoding a synaptic protein					
a39-Takusan (Alpha39-takusan)	EF651836	2.30	1.39E-07	10417411	Tu et al., 2007

Fold change reflects the expression level of the gene in the organ of Corti of *Pjvk*$^{-/-}$ relative to *Pjvk*$^{+/+}$ mice. + and - denote up-regulation and down-regulation, respectively. The p values were adjusted using the Benjamini-Hochberg algorithm.

Figure 1

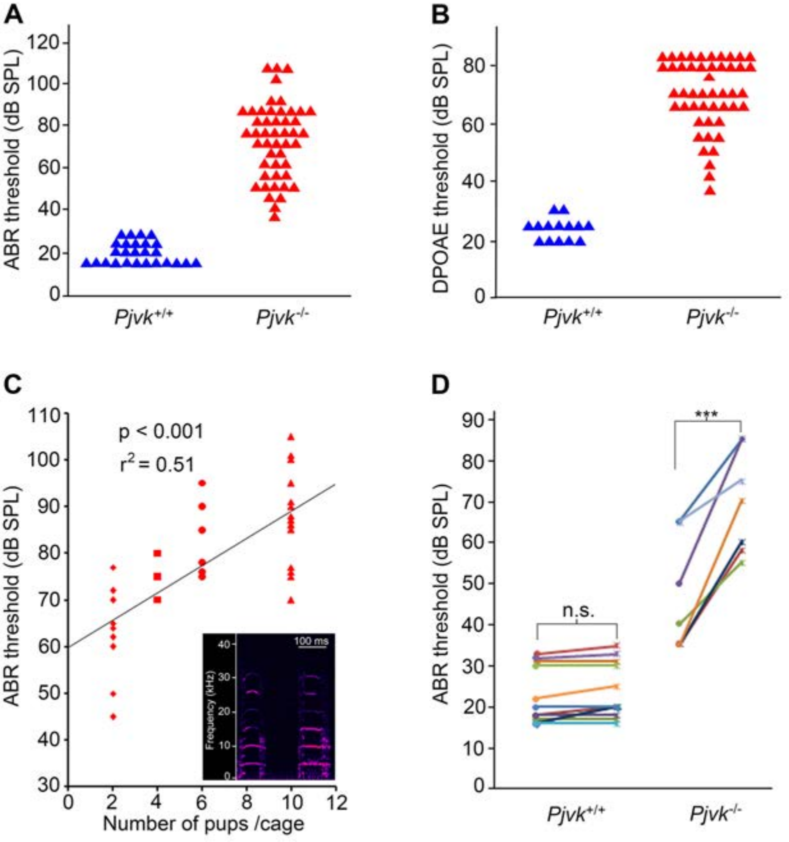
A
ABR threshold (dB SPL)
0
20
40
60
80
100
120
$Pjvk^{+/+}$
$Pjvk^{-/-}$
B
DPOAE threshold (dB SPL)
0
20
40
60
80
$Pjvk^{+/+}$
$Pjvk^{-/-}$
C
$p < 0.001$
$r^2 = 0.51$
ABR threshold (dB SPL)
30
40
50
60
70
80
90
100
110
0
2
4
6
8
10
12
Number of pups /cage
Frequency (kHz)
0
10
20
30
40
100 ms
D
ABR threshold (dB SPL)
0
10
20
30
40
50
60
70
80
90
n.s.
***
$Pjvk^{+/+}$
$Pjvk^{-/-}$

Figure 2

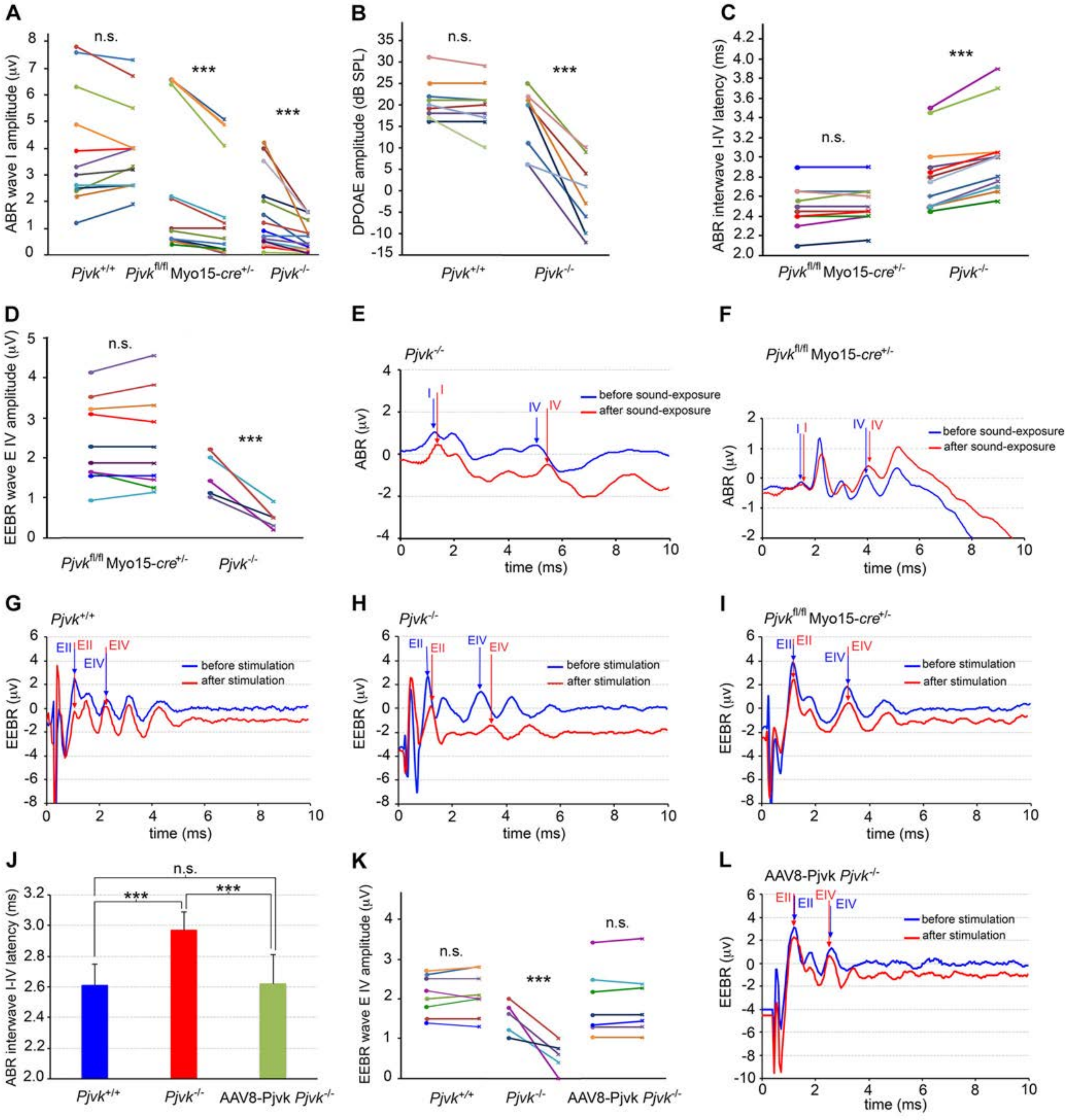
A
ABR wave I amplitude (μv)
n.s.
***
***
Pjvk$^{+/+}$
Pjvk$^{fl/fl}$ Myo15-*cre*$^{+/-}$
Pjvk$^{-/-}$
B
DPOAE amplitude (dB SPL)
n.s.
***
Pjvk$^{+/+}$
Pjvk$^{-/-}$
C
ABR interwave I-IV latency (ms)
n.s.
***
Pjvk$^{fl/fl}$ Myo15-*cre*$^{+/-}$
Pjvk$^{-/-}$
D
EEBR wave E IV amplitude (μV)
n.s.
***
Pjvk$^{fl/fl}$ Myo15-*cre*$^{+/-}$
Pjvk$^{-/-}$
E
Pjvk$^{-/-}$
ABR (μv)
I
I
IV
IV
before sound-exposure
after sound-exposure
time (ms)
F
Pjvk$^{fl/fl}$ Myo15-*cre*$^{+/-}$
ABR (μv)
I
I
IV
IV
before sound-exposure
after sound-exposure
time (ms)
G
Pjvk$^{+/+}$
EEBR (μv)
EII
EII
EIV
EIV
before stimulation
after stimulation
time (ms)
H
Pjvk$^{-/-}$
EEBR (μv)
EII
EII
EIV
EIV
before stimulation
after stimulation
time (ms)
I
Pjvk$^{fl/fl}$ Myo15-*cre*$^{+/-}$
EEBR (μv)
EII
EII
EIV
EIV
before stimulation
after stimulation
time (ms)
J
ABR interwave I-IV latency (ms)
n.s.
***
***
Pjvk$^{+/+}$
Pjvk$^{-/-}$
AAV8-Pjvk *Pjvk*$^{-/-}$
K
EEBR wave E IV amplitude (μV)
n.s.
***
n.s.
Pjvk$^{+/+}$
Pjvk$^{-/-}$
AAV8-Pjvk *Pjvk*$^{-/-}$
L
AAV8-Pjvk *Pjvk*$^{-/-}$
EEBR (μv)
EII
EII
EIV
EIV
before stimulation
after stimulation
time (ms)

Figure 3

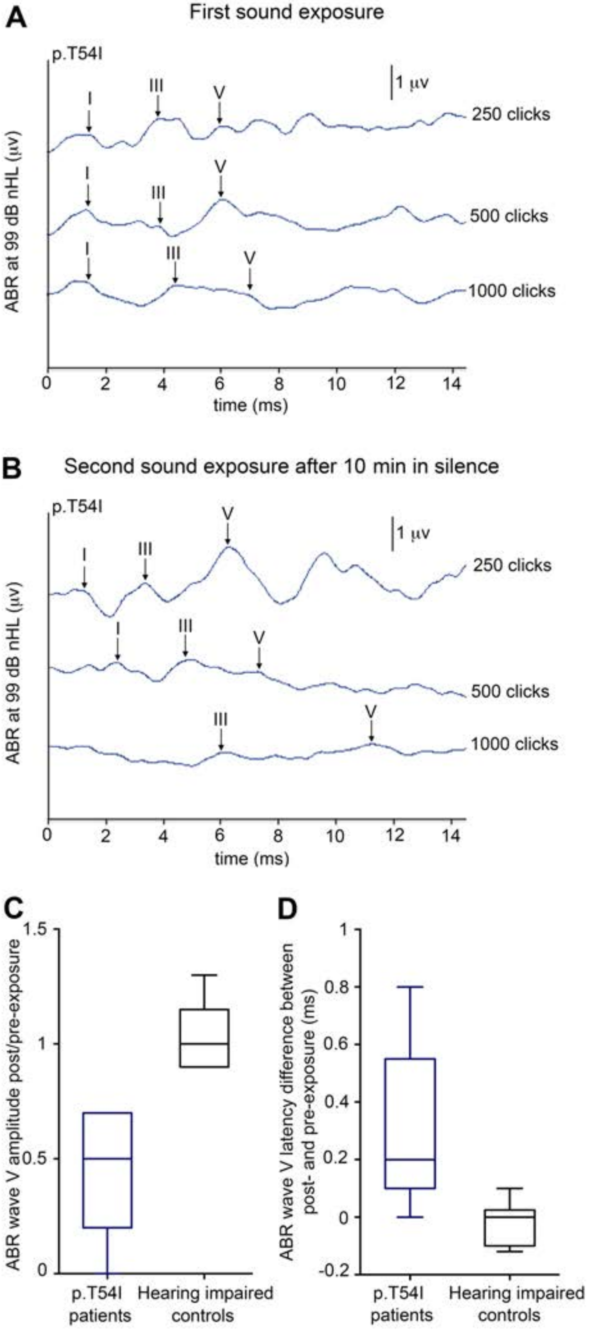
A
First sound exposure
p.T54I
ABR at 99 dB nHL (µv)
1 µv
I
III
V
250 clicks
500 clicks
1000 clicks
0
2
4
6
8
10
12
14
time (ms)
B
Second sound exposure after 10 min in silence
p.T54I
ABR at 99 dB nHL (µv)
1 µv
I
III
V
250 clicks
500 clicks
1000 clicks
0
2
4
6
8
10
12
14
time (ms)
C
ABR wave V amplitude post/pre-exposure
1.5
1
0.5
0
p.T54I patients
Hearing impaired controls
D
ABR wave V latency difference between post- and pre-exposure (ms)
1
0.8
0.6
0.4
0.2
0
-0.2
p.T54I patients
Hearing impaired controls

Figure 4

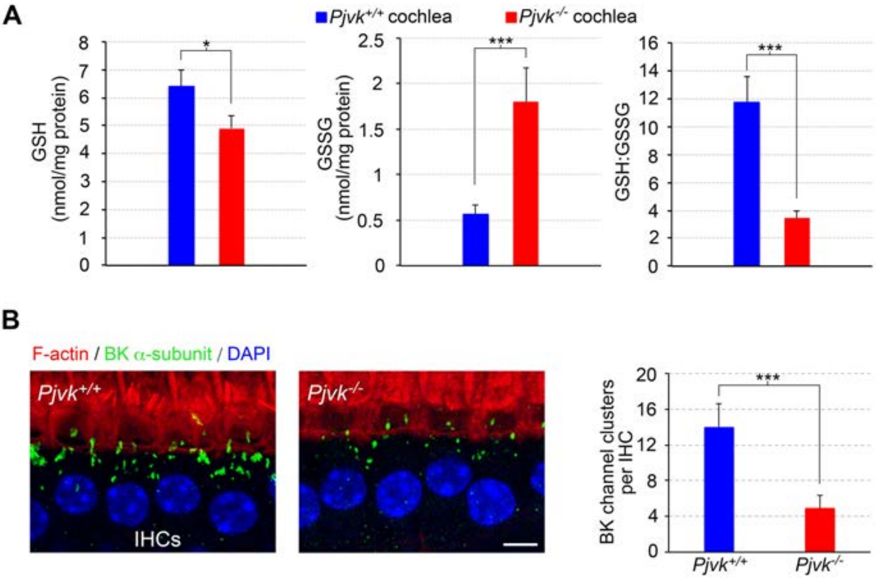
A
Pjvk+/+ cochlea
Pjvk-/- cochlea
GSH (nmol/mg protein)
0
1
2
3
4
5
6
7
8
*
GSSG (nmol/mg protein)
0
0.5
1
1.5
2
2.5
***
GSH:GSSG
0
2
4
6
8
10
12
14
16
***
B
F-actin / BK α-subunit / DAPI
Pjvk+/+
IHCs
Pjvk-/-
BK channel clusters per IHC
0
4
8
12
16
20
***
Pjvk+/+
Pjvk-/-

Figure 5

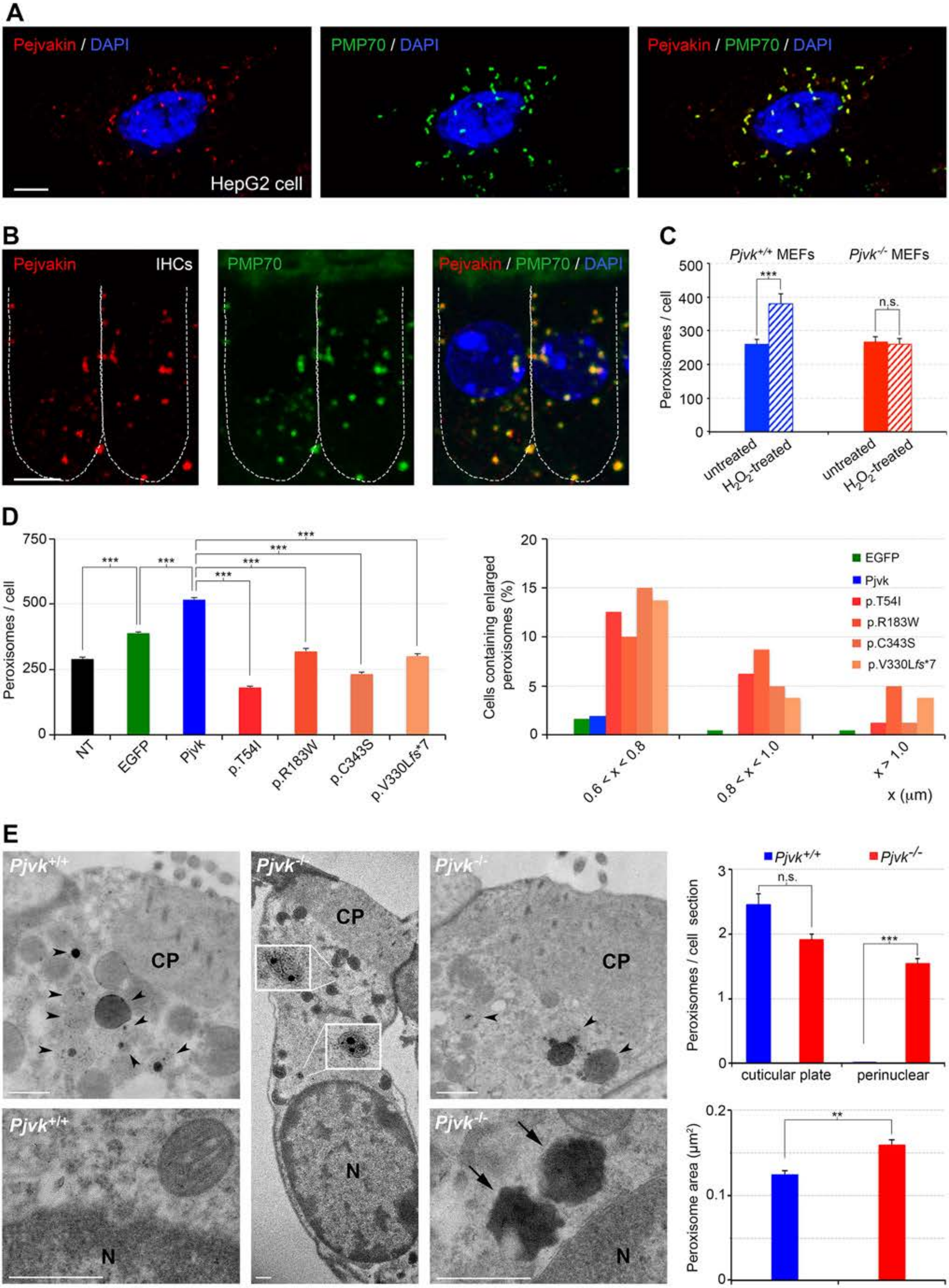
A
Pejvakin / DAPI
HepG2 cell
PMP70 / DAPI
Pejvakin / PMP70 / DAPI
B
Pejvakin
IHCs
PMP70
Pejvakin / PMP70 / DAPI
C
Pjvk+/+ MEFs
Pjvk-/- MEFs
Peroxisomes / cell
500
400
300
200
100
0
***
n.s.
untreated
H2O2-treated
untreated
H2O2-treated
D
750
500
250
0
Peroxisomes / cell
***
***
***
***
***
***
NT
EGFP
Pjvk
p.T54I
p.R183W
p.C343S
p.V330Lfs*7
20
15
10
5
0
Cells containing enlarged peroxisomes (%)
EGFP
Pjvk
p.T54I
p.R183W
p.C343S
p.V330Lfs*7
0.6 < x < 0.8
0.8 < x < 1.0
x > 1.0
x (μm)
E
Pjvk+/+
CP
Pjvk-/-
CP
N
Pjvk-/-
CP
Pjvk+/+
N
Pjvk-/-
N
Pjvk+/+
Pjvk-/-
3
2
1
0
Peroxisomes / cell section
n.s.
***
cuticular plate
perinuclear
0.2
0.1
0
Peroxisome area (μm2)
**

Figure 6

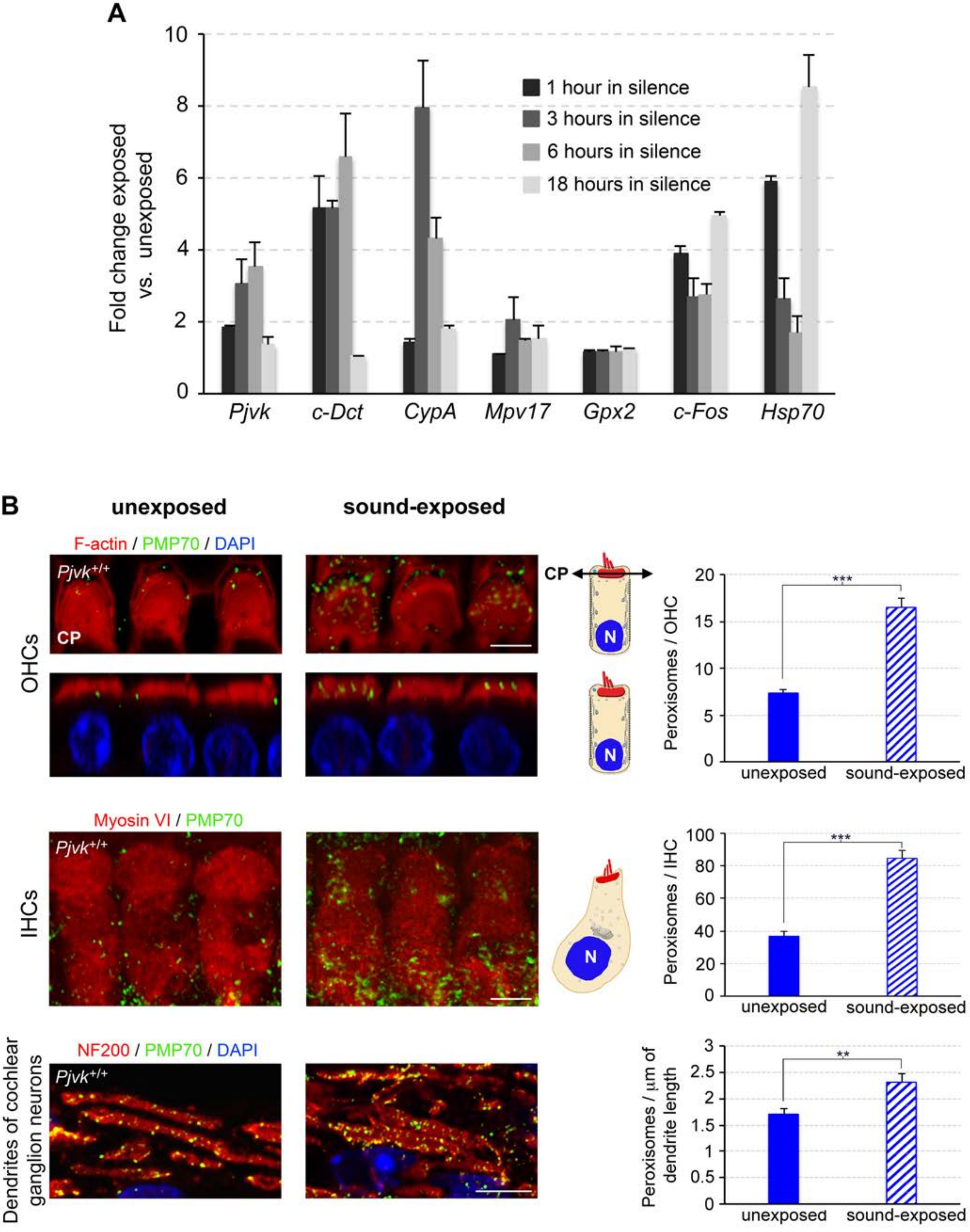
A
Fold change exposed vs. unexposed
0
2
4
6
8
10
1 hour in silence
3 hours in silence
6 hours in silence
18 hours in silence
Pjvk
c-Dct
CypA
Mpv17
Gpx2
c-Fos
Hsp70
B
unexposed
sound-exposed
F-actin / PMP70 / DAPI
Pjvk+/+
CP
OHCs
CP
N
N
Peroxisomes / OHC
0
5
10
15
20
***
unexposed
sound-exposed
Myosin VI / PMP70
Pjvk+/+
IHCs
N
Peroxisomes / IHC
0
20
40
60
80
100
***
unexposed
sound-exposed
NF200 / PMP70 / DAPI
Pjvk+/+
Dendrites of cochlear ganglion neurons
Peroxisomes / µm of dendrite length
0
0.5
1
1.5
2
2.5
3
**
unexposed
sound-exposed

Figure 7

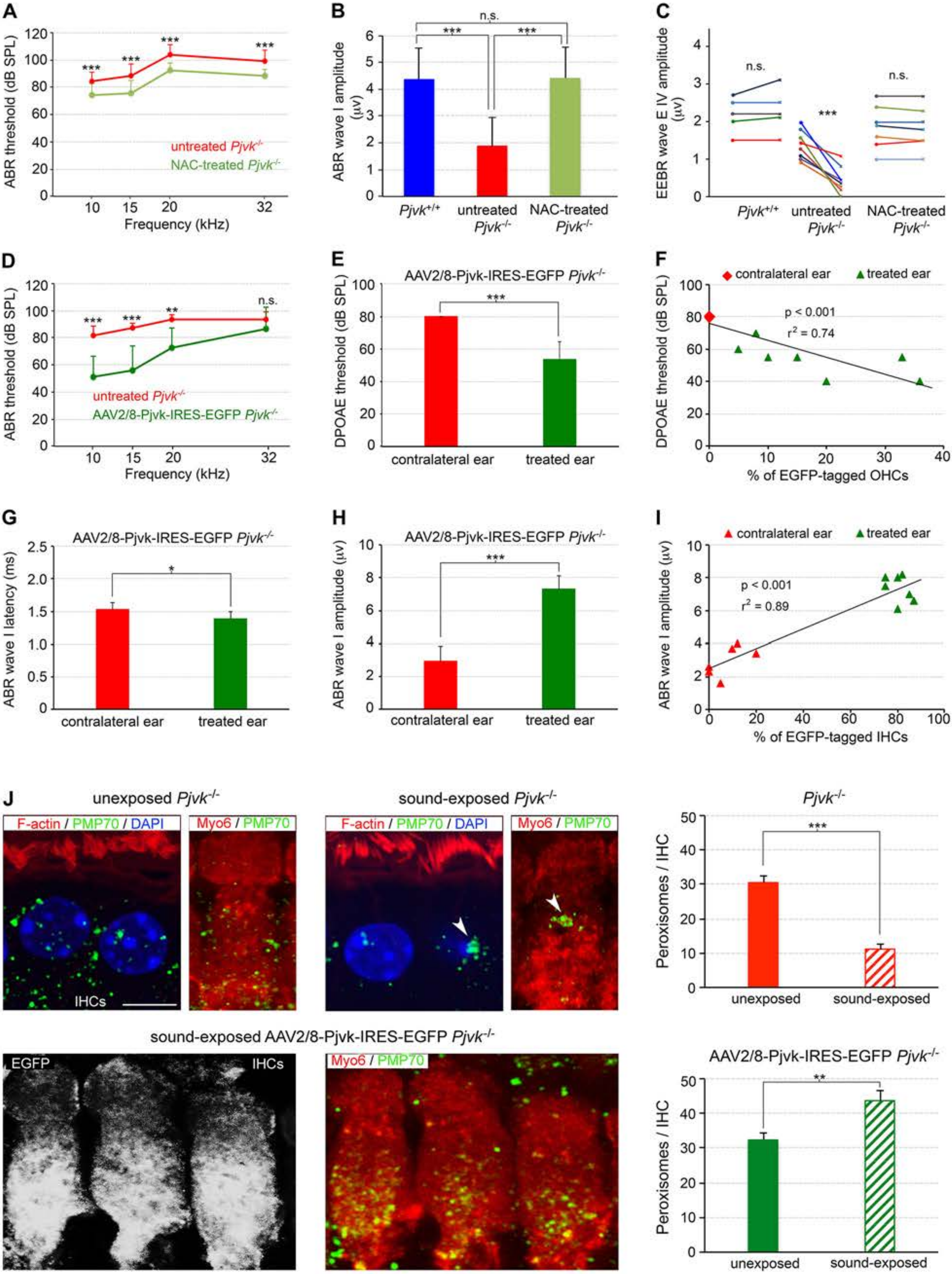
A
ABR threshold (dB SPL)
120
100
80
60
40
20
0
***
***
***
***
untreated Pjvk-/-
NAC-treated Pjvk-/-
10
15
20
32
Frequency (kHz)
B
n.s.
***
***
ABR wave I amplitude (μv)
6
5
4
3
2
1
0
Pjvk+/+
untreated Pjvk-/-
NAC-treated Pjvk-/-
C
EEBR wave E IV amplitude (μv)
4
3
2
1
0
n.s.
***
n.s.
Pjvk+/+
untreated Pjvk-/-
NAC-treated Pjvk-/-
D
ABR threshold (dB SPL)
120
100
80
60
40
20
0
***
***
**
n.s.
untreated Pjvk-/-
AAV2/8-Pjvk-IRES-EGFP Pjvk-/-
10
15
20
32
Frequency (kHz)
E
AAV2/8-Pjvk-IRES-EGFP Pjvk-/-
DPOAE threshold (dB SPL)
100
80
60
40
20
0
***
contralateral ear
treated ear
F
◆ contralateral ear
▲ treated ear
DPOAE threshold (dB SPL)
100
80
60
40
20
0
p < 0.001
r2 = 0.74
0
10
20
30
40
% of EGFP-tagged OHCs
G
AAV2/8-Pjvk-IRES-EGFP Pjvk-/-
ABR wave I latency (ms)
2.5
2.0
1.5
1.0
0.5
0
*
contralateral ear
treated ear
H
AAV2/8-Pjvk-IRES-EGFP Pjvk-/-
ABR wave I amplitude (μv)
10
8
6
4
2
0
***
contralateral ear
treated ear
I
▲ contralateral ear
▲ treated ear
ABR wave I amplitude (μv)
10
8
6
4
2
0
p < 0.001
r2 = 0.89
0
20
40
60
80
100
% of EGFP-tagged IHCs
J
unexposed Pjvk-/-
F-actin / PMP70 / DAPI
Myo6 / PMP70
IHCs
sound-exposed Pjvk-/-
F-actin / PMP70 / DAPI
Myo6 / PMP70
Pjvk-/-
Peroxisomes / IHC
50
40
30
20
10
0
***
unexposed
sound-exposed
sound-exposed AAV2/8-Pjvk-IRES-EGFP Pjvk-/-
EGFP
IHCs
Myo6 / PMP70
AAV2/8-Pjvk-IRES-EGFP Pjvk-/-
Peroxisomes / IHC
50
40
30
20
10
0
**
unexposed
sound-exposed

Figure S1

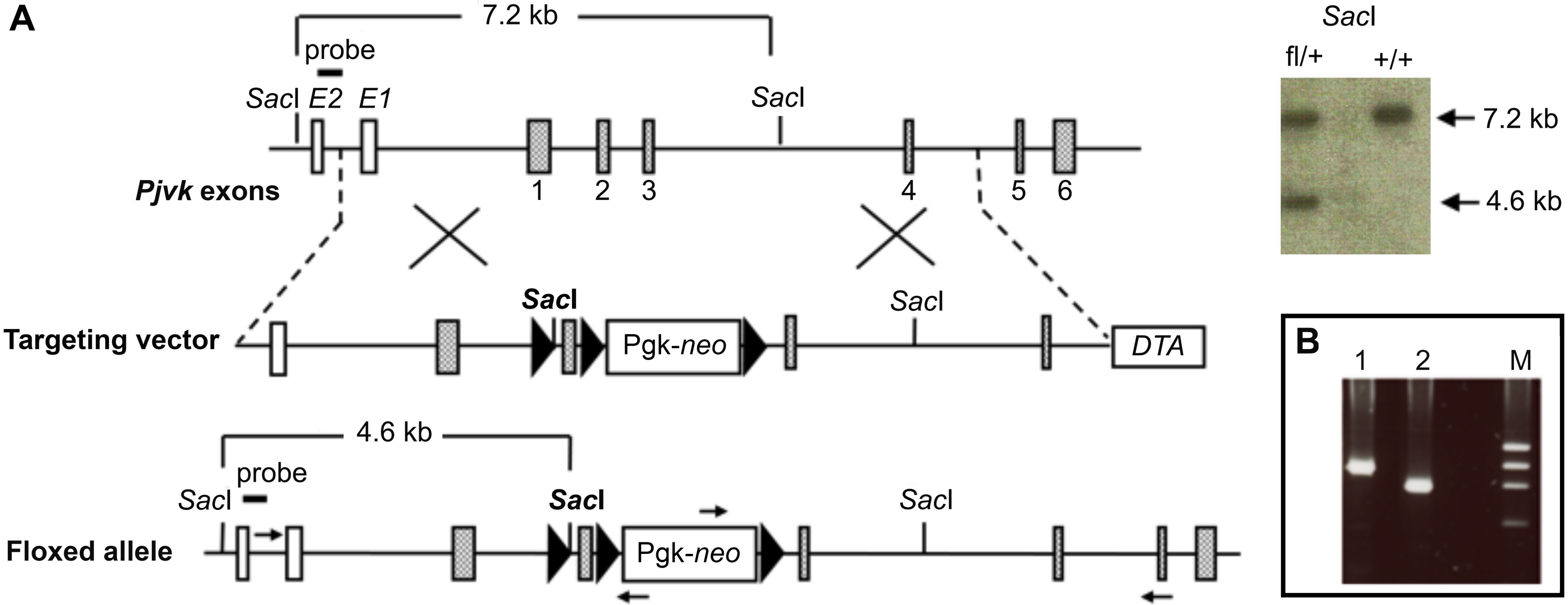
A
7.2 kb
probe
SacI E2 E1
SacI
Pjvk exons
1 2 3 4 5 6
SacI
Targeting vector
Pgk-neo
SacI
DTA
4.6 kb
probe
SacI
SacI
SacI
Floxed allele
Pgk-neo
SacI
fl/+ +/+
7.2 kb
4.6 kb
B
1 2 M

Figure S2

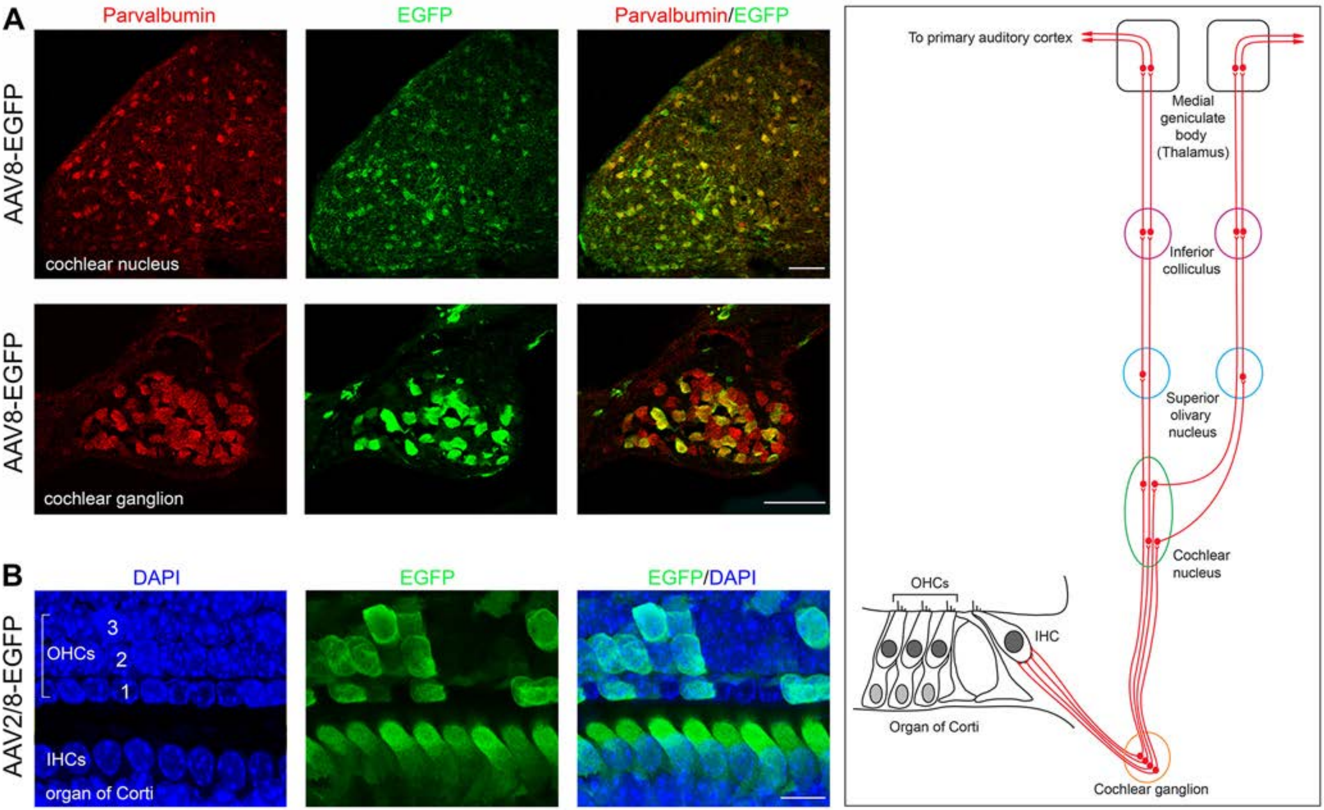
A
Parvalbumin
EGFP
Parvalbumin/EGFP
AAV8-EGFP
cochlear nucleus
AAV8-EGFP
cochlear ganglion
B
DAPI
EGFP
EGFP/DAPI
AAV2/8-EGFP
OHCs
3
2
1
IHCs
organ of Corti
To primary auditory cortex
Medial geniculate body (Thalamus)
Inferior colliculus
Superior olivary nucleus
Cochlear nucleus
OHCs
IHC
Organ of Corti
Cochlear ganglion

Figure S3

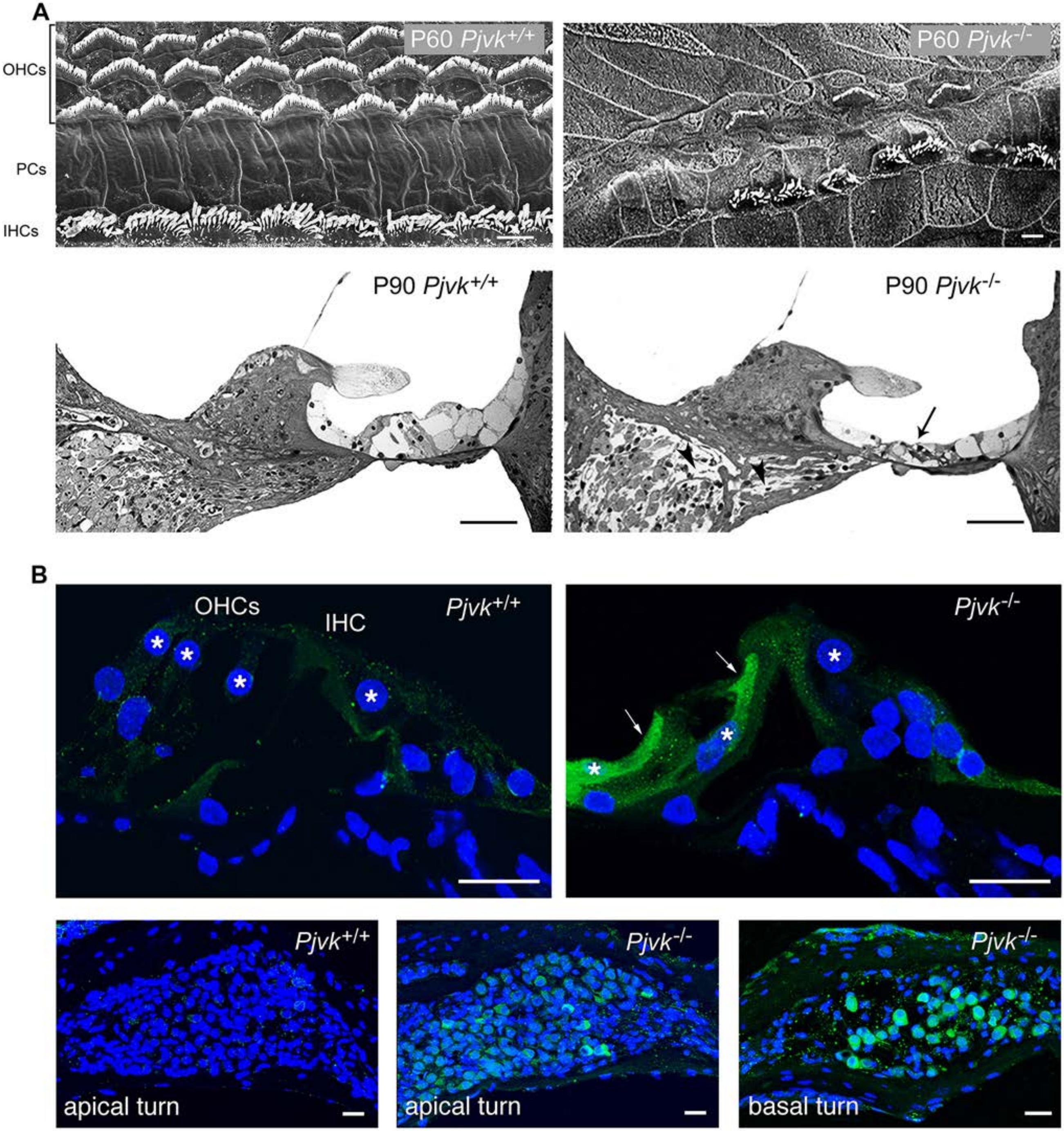
A
OHCs
PCs
IHCs
P60 *Pjvk*$^{+/+}$
P60 *Pjvk*$^{-/-}$
P90 *Pjvk*$^{+/+}$
P90 *Pjvk*$^{-/-}$
B
OHCs
IHC
Pjvk$^{+/+}$
Pjvk$^{-/-}$
Pjvk$^{+/+}$
apical turn
Pjvk$^{-/-}$
apical turn
Pjvk$^{-/-}$
basal turn

Figure S4

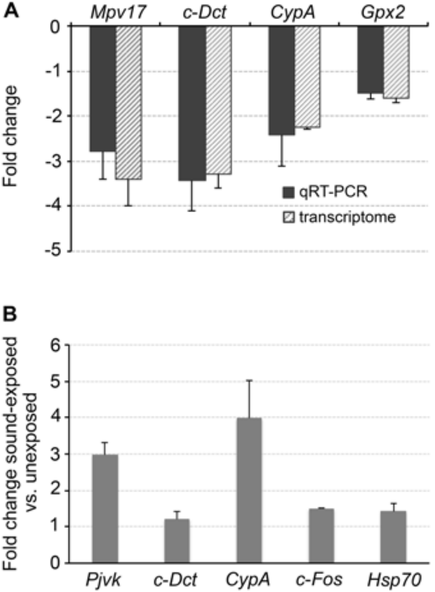
A
Mpv17
c-Dct
CypA
Gpx2
0
-1
-2
-3
-4
-5
Fold change
qRT-PCR
transcriptome
B
Fold change sound-exposed vs. unexposed
6
5
4
3
2
1
0
Pjvk
c-Dct
CypA
c-Fos
Hsp70

Figure S5

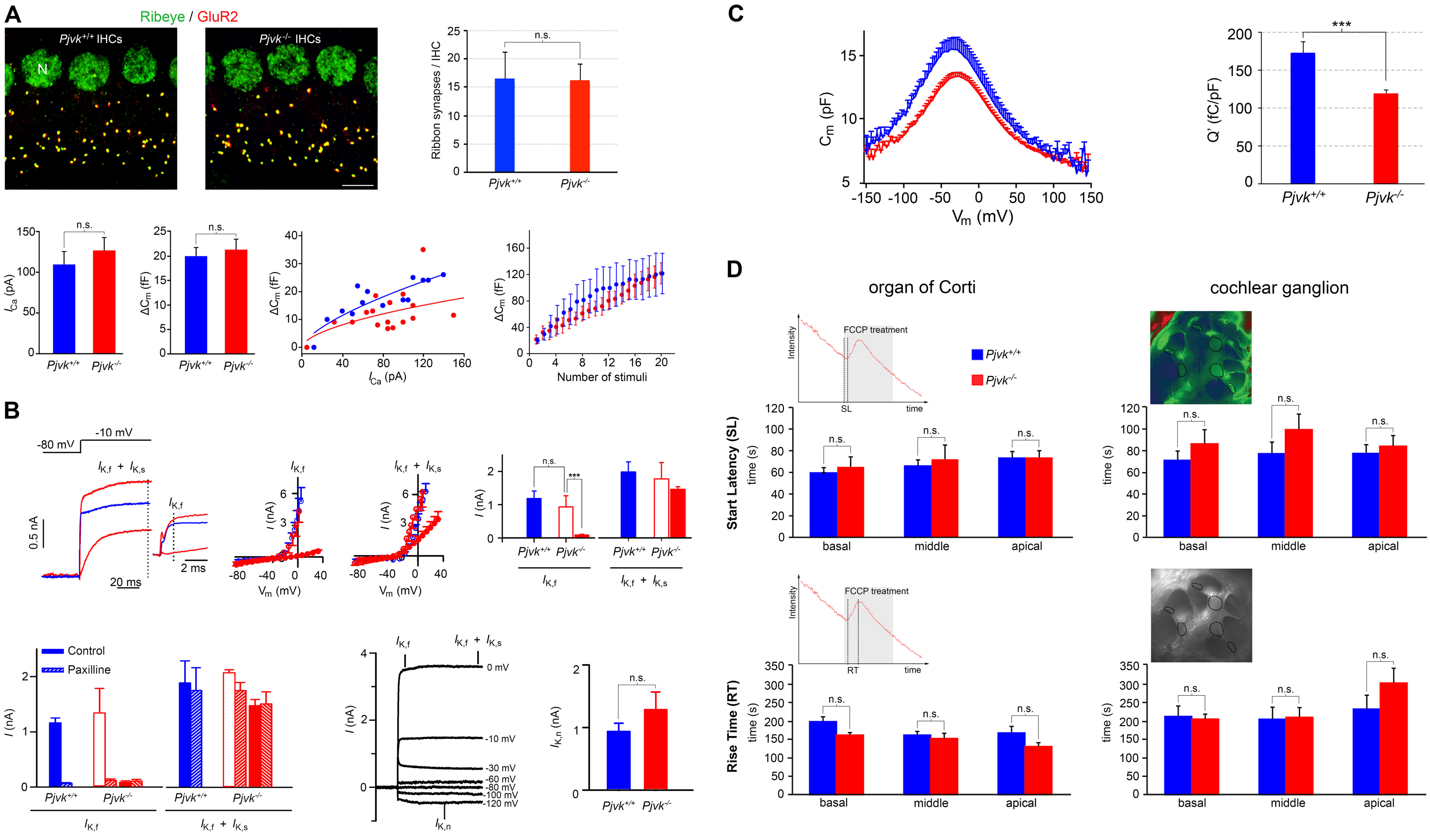
A
Ribeye / GluR2
Pjvk+/+ IHCs
N
Pjvk-/- IHCs
Ribbon synapses / IHC
n.s.
Pjvk+/+
Pjvk-/-
I_Ca (pA)
ΔC_m (fF)
I_Ca (pA)
Number of stimuli
B
-80 mV
-10 mV
I_K,f + I_K,s
I_K,f
0.5 nA
20 ms
2 ms
V_m (mV)
I (nA)
***
Control
Paxilline
0 mV
-10 mV
-30 mV
-60 mV
-80 mV
-100 mV
-120 mV
I_K,n
I_K,n (nA)
C
C_m (pF)
V_m (mV)
Q' (fC/pF)
D
organ of Corti
cochlear ganglion
Intensity
FCCP treatment
SL
RT
time
Start Latency (SL)
Rise Time (RT)
time (s)
basal
middle
apical

Figure S6

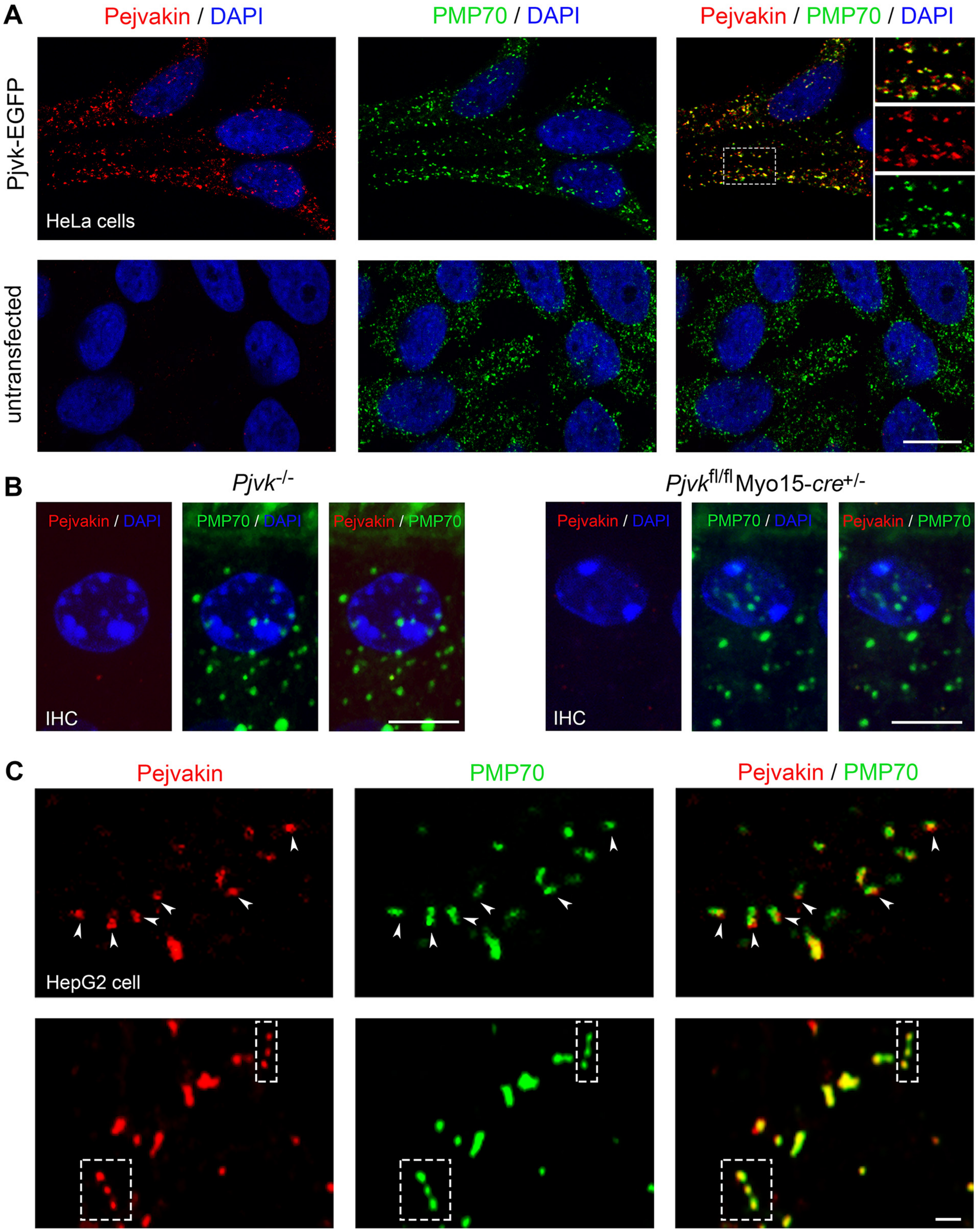
A
Pejvakin / DAPI
PMP70 / DAPI
Pejvakin / PMP70 / DAPI
Pjvk-EGFP
HeLa cells
untransfected
B
Pjvk-/-
Pjvkfl/fl Myo15-cre+/-
Pejvakin / DAPI
PMP70 / DAPI
Pejvakin / PMP70
IHC
C
Pejvakin
PMP70
Pejvakin / PMP70
HepG2 cell

Figure S7

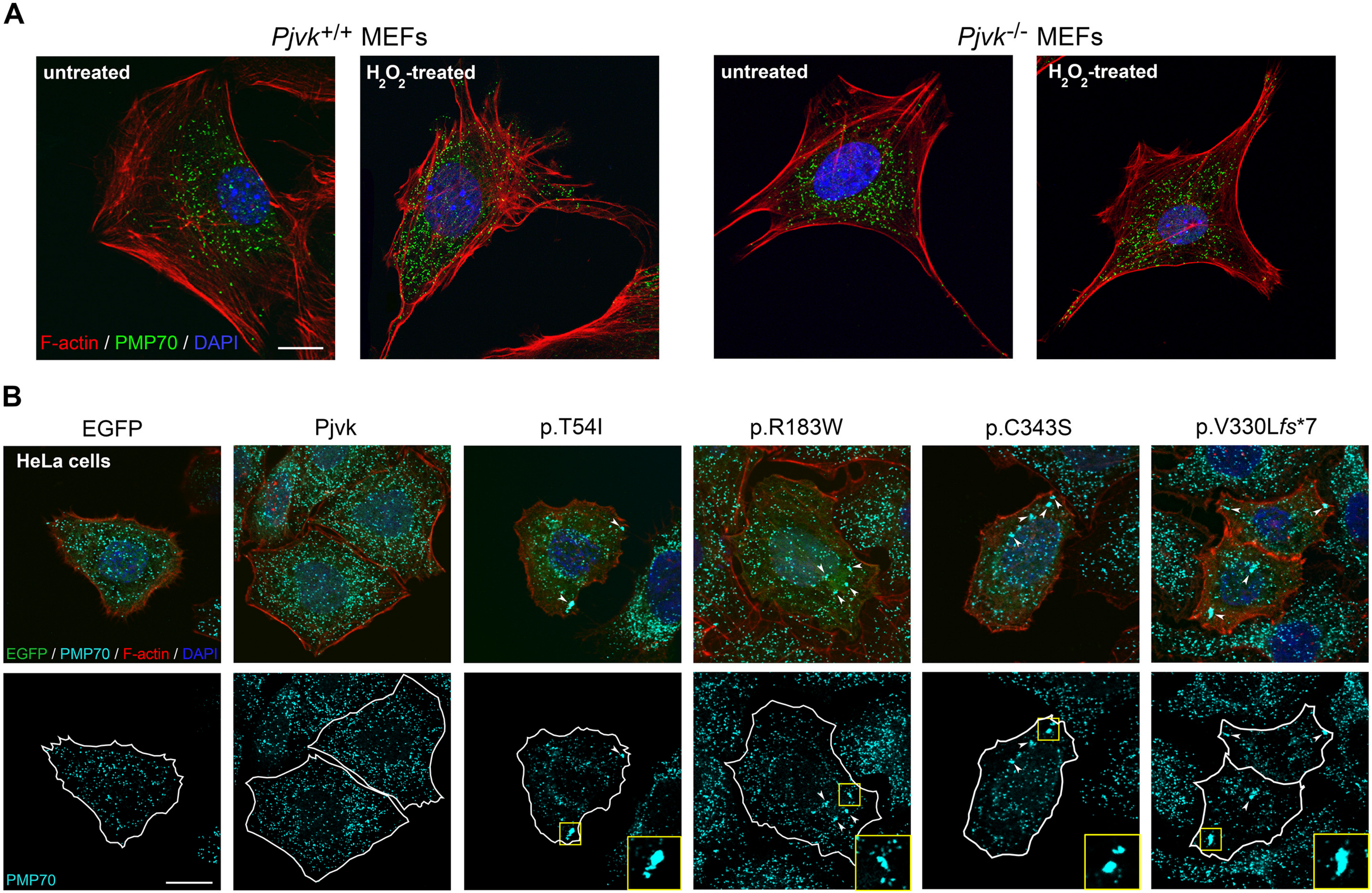
A
Pjvk+/+ MEFs
Pjvk-/- MEFs
untreated
H2O2-treated
untreated
H2O2-treated
F-actin / PMP70 / DAPI
B
EGFP
Pjvk
p.T54I
p.R183W
p.C343S
p.V330Lfs*7
HeLa cells
EGFP / PMP70 / F-actin / DAPI
PMP70